On the assessment of sinking particle fluxes from in situ particle size distributions

Draft date: December 16, 2024

Authors: Elena Ceballos Romero[1,2,*], Ken Buesseler[1], Erik Fields[3], Rainer Kiko[4,5,6], Meg Estapa[7], Lee Karp-Boss[8], Samantha Clevenger[9], Laetitia Drago[4], David A. Siegel[3,10]

[1]Woods Hole Oceanographic Institution, Department of Marine Chemistry & Geochemistry, Woods Hole, Massachusetts (USA),

[2]Department of Applied Physics II, University of Sevilla, Av. Reina Mercedes 4A, 41012, Sevilla, Spain

[3]Earth Research Institute, University of California, Santa Barbara, Santa Barbara, California (USA),

[4]Sorbonne Université, Laboratoire d'Océanographie de Villefranche, Villefranche-sur-Mer (France)

[5]GEOMAR Helmholtz Centre for Ocean Research Kiel, Kiel, Germany

[6]Faculty of Mathematics and Natural Sciences, University of Kiel, 24148 Kiel, Germany

[7]School of Marine Sciences, University of Maine, Darling Marine Center, Walpole, Maine (USA)

[8]School of Marine Sciences, University of Maine, Orono, Maine (USA)

[9]MIT-WHOI Joint Program in Oceanography, Applied Ocean Science and Engineering, Cambridge, MA, (USA)

[10]Department of Geography, University of California, Santa Barbara, Santa Barbara, California (USA)

Corresponding author: Elena Ceballos Romero (eceballos@whoi.edu)

Abstract

The biological carbon pump plays a crucial role in the global carbon cycle, particularly through sinking particles carrying carbon to deep waters. The Underwater Vision Profilers (UVP) is widely used for studying particle properties. UVP-based particulate organic carbon (POC) flux is typically derived from particle size distributions (PSDs) assuming size dependent sinking rates and carbon content. This approach, the "classic UVP method", calibrates PSD-based flux against sediment trap flux data that are not necessarily co-located in space or time. We put forth a "modified UVP method" that combines a large data set of UVP measurements calibrated against POC flux from co-located and simultaneously collected sediment traps and thorium-234 measurements. Data were collected in the North Pacific (50°N, 145°W, August 2018) and the North Atlantic (49°N, 16.5°W, May 2021) as part of EXPORTS (EXport Processes in the Ocean from RemoTe Sensing), covering a wide range of environmental conditions. We find that our modified UVP methods explain 80% of the variance in POC flux when applied across sites, where flux values vary over orders of magnitude. However, the method fails to account for smaller flux variations within a single site or across depths. Reasons include undersampling rare large particles, mismatch in time and spatial scales of UVPs calibrated against fluxes in traps and ^{234}Th, and difficulties in interpreting particle stock and flux changes within non-steady state conditions. To use UVP as a high-resolution POC flux tool, it is recommended not to rely on a few profiles for calibration.

Keywords: biological carbon pump, sinking carbon export fluxes, particle imaging, sediment traps, thorium-234, ocean carbon cycle.

1 Introduction

The oceanic biological carbon pump (BCP) (Eppley & Peterson, 1979) drives carbon storage in the ocean's interior through the downward flux of biogenic carbon, produced by the net primary production of phytoplankton. There are multiple paths for the BCP (Boyd et al., 2019) but when considering transport to the deep ocean (>1000m) this process occurs primarily through the gravitational sinking of Particulate Organic Carbon (POC) - phytoplankton, zooplankton, detritus, and fecal pellets - form the euphotic zone to deep waters (Boyd et al., 2019; Turner, 2002; Turner, 2015). While the BCP significantly impacts atmospheric CO_2 over geological timescales (De La Rocha & Passow, 2007), its current role in the global carbon cycle, particularly in response to human-induced changes, remains uncertain. Annual carbon export estimates by the BCP vary from 5 to >12 Gt C yr^{-1} (Boyd & Trull, 2007; Henson et al., 2011).

Traditional oceanographic techniques like sediment traps (e.g., Buesseler et al., 2007) or radioactive disequilibrium methods such as thorium-234 (^{234}Th half-life, $t_{½}$ = 24.1 d; e.g., Buesseler et al., 1992), are resource-intensive and provide limited spatial, vertical, and temporal coverage (Buesseler et al., 2007). The emergence of imaging techniques in recent decades has transformed oceanography (Lombard & Kiørboe, 2010), offering a range of tools to study properties and dynamics of particles across a range of sizes, from micrometers to centimeters, and time scales of seconds depending upon imaging protocols. These techniques, deployable on CTD rosettes from research vessels, autonomous floats, gliders, or moorings, enable observations on oceanographically relevant temporal and spatial scales, while at the same time reducing deployment costs (Giering et al., 2020). Among these, the Underwater Vision Profiler or UVP (Picheral et al., 2010) has become one of the most widely used imaging techniques because of its versatility (Kiko et al., 2022; Picheral et al., 2022).

In situ observations of particle size distributions (PSD) from imaging platforms historically served three main purposes: 1) gaining knowledge of plankton, as PSD of the living fraction offers insights into the structural properties of marine food webs and various ecological processes (Sheldon et al., 1972); 2) inferring sinking velocities of individual particle size classes when combined with particle collection traps equipped with polyacrylamide gels (McDonnell & Buesseler, 2010); and 3) estimating sinking particles fluxes when PSD is combined with conventional sediment trap measurements to derive particle properties that correlate PSD with

independent flux data. This approach was pioneered by Guidi et al. (2008) and applied by others (e.g., Iversen et al. 2010; Kiko et al. 2017). In this study, we revisit and expand this third application of PSD but, in this case, using a local calibration of flux against both traps and ^{234}Th approaches. Each of these methods has their strengths and weaknesses including the spatial and temporal scales each represents. Here, we test the assumption that an instantaneous PSD imaged by UVP, essentially a stock measurement, can be related to POC flux, a rate of carbon removal on gravitationally sinking particles.

We refer to the method first proposed by Guidi et al. (2008) as the "classic UVP method" where the UVP retrieved PSD is used to estimate mass fluxes constrained by sediment trap observations of the sinking POC flux. The classic method assumes that the total mass flux (e.g., POC) can be theoretically estimated from PSDs by integrating the flux spectrum over all particle diameters (D), or:

$$POC_{flux} = \int_{D_{min}}^{D_{max}} N(D)\, \rho_{POC}(D)\, w_s(D) \qquad \text{Eq. (1),}$$

where $N(D)$ is the number concentration of particles as a function of size in differential form (# L^{-1} mm^{-1}), ρ_{POC} is the POC content of an individual particle (mg C $particle^{-1}$), w_s is its sinking rate (m s^{-1}), and D_{min} and D_{max} are the smallest and largest particle sizes resolved, respectively (mm). However, we do not a priori know particle sinking rates and POC content, and even if we did, they are not likely to be uniform within a given size class (Laurenceau-Cornec et al., 2015).

Hence, Eq. (1) is often reformulated by combining the POC content and sinking rate terms into a power function of particle diameter (Alldredge, 1998; Alldredge & Gotschalk, 1988; Lombard & Kiørboe, 2010), resulting in:

$$POC_{flux} = \int_{D_{min}}^{D_{max}} N(D)\, A\, D^B dD \qquad \text{Eq. (2),}$$

Guidi et al. (2008) calculated POC flux using PSDs retrieved from UVPs, with A and B coefficients optimized using available sinking particle flux observations. The wide application of this approach assumes that the power law constants are valid globally.

Coefficient A represents the product of sinking speed and POC content, while coefficient B, is linked to the fractal dimension, which describes particle shape complexity. Under fractal scaling, where that POC content and sinking speed spectra are mathematically described by power-law

relationships with particle size, the value of B represents the slope of the product of POC and sinking speed and is related to the fractal dimension (Guidi et al., 2008; Logan & Wilkinson, 1990). Changes in B reflect changes in *F* and the physical characteristics of particles, such as porosity or how they aggregate together as they sink through the water column. A lower fractal dimension (smaller B coefficient) suggests a more rugged particle, with more intricate structures and higher porosity, whereas a larger B indicates a smoother, more compact, nearly spherical shape. However, this relationship is idealized, and in practice, the fit value of B is influenced by factors such as the size range, instrument resolution, and specific image processing methodologies used in Bisson et al. (2022).

In developing the classic UVP method, Guidi et al. (2008) compared UVP observations to a set of moored and drifting sediment trap fluxes collected across different studies. However, the trap and UVP observations were not consistently co-located, nor were they deployed in the same season or at the same depth, as only a few UVP profiles were taken in conjunction with sediment trap deployments. Trap data were collected from a few sites in the North Atlantic Ocean, Mediterranean Sea and South Pacific Ocean (see Guidi et al. (2008), Table 3), while the UVP data were from a much broader set of sites and studies (see Guidi et al. (2008), Figure 1).

Since the introduction of this classic UVP method, the A and B coefficients from Guidi et al. (2008) have been used for the prediction of POC flux in many studies without much questioning (e.g., (Forest et al., 2013; Guidi et al., 2009, 2015, 2016; Ramondenc et al., 2016). Only Iversen et al. (2010) and Fender et al. (2019) estimated A and B coefficients following the classic UVP method using co-located deep sediment trap fluxes off the Mauritanian coast and the California Current Ecosystem, respectively. More recently, Clements et al. (2023) estimated A and B using a machine learning reconstruction of global ocean PSDs from UVPs measurements tuned against a global compilation of in situ sediment trap and thorium-derived particle flux observations.

In this study, we use a comprehensive and unique dataset of PSD observations from UVPs, along with POC flux estimates from sediment traps and thorium-234 (^{234}Th) that were co-located in space and time, to evaluate the performance and validity of the classic UVP method. We refer to this as the "modified UVP method" henceforth in this paper, a distinguishing feature being the application of a local calibration of A and B for a given set of UVP data. These UVP and co-located flux data were collected together as part of the NASA-funded EXport Processes in the

Ocean from RemoTe Sensing (EXPORTS) project at two biogeochemically contrasting sites in terms of POC flux and biogeochemical conditions (Siegel et al., 2024, 2021). This modified method allows us to better quantify POC flux differences between widely varying flux settings in the NP and NA, but fails to account for regional flux variations within a single site or as it changes with depth.

2 Materials and Methods

2.1 Settings

The goal of the EXPORTS field campaign is to develop a predictive understanding of the export, fate, and C cycle impacts of global ocean net primary production and to assess their impacts in contemporary and future climates (Siegel et al., 2016). Two field campaigns were carried out in two vastly different ocean ecosystems encompassing a wide range of environmental conditions: 1) the North Pacific (NP) at Ocean Station Papa (OSP, 50°N, 145°W) in August-September 2018, and 2) the North Atlantic (NA) in the vicinity of the Porcupine Abyssal Plains Sustained Observatory (PAP, 49°N, 16.5°W) in May 2021. In both field deployments, operations were conducted in three consecutive sampling cycles or "epochs" (E1, E2, and E3 from hereafter) designed to constrain the pathways for organic carbon transformation and export. The length of each epoch was approximately one week with the goal of completing a sequence of observations that could be repeated three times during a given cruise. Conceptually, the aim is to follow how surface properties might be observed to propagate to depth as part of the BCP, i.e., a particle formed at the surface on day 1, would take approximately one week to reach 500 m if settling at roughly 70 m/d (Siegel et al., 2021).

2.1.1 North Pacific (OSP, Aug-Sep 2018)

OSP (50°N, 145°W) can be characterized as an iron-limited, high-nutrient, low-chlorophyll (HNLC) regions of the world ocean, which leads to limited phytoplankton production and surface chlorophyll (Chl-a) concentrations. An overview of the NP sampling plan, including context information on physical and bio-optical properties, nutrients, and phytoplankton biomass, is presented in Siegel et al. (2021). Briefly, during our study period the oceanographic setting was typical of late-summer conditions at OSP with low biomass, a highly recycled food web, and low sinking POC export fluxes driven by largely zooplankton processes (Stamieszkin et al., 2021; Steinberg et al., 2023). Weak horizontal currents and spatial gradients in biogeochemical fields

and low level of temporal variability characterized the three sampling epochs (E): E1 (August 14-23), E2 (August 24-31), and E3 (September 1-9). In terms of POC export, the site was characterized by a modest sinking carbon fluxes with an export efficiency at the base of the euphotic zone of 13% + 5% (ratio of POC flux to net primary production) and 39% flux attenuation in the subsequent 100 m (Buesseler et al., 2020).

2.1.2 North Atlantic (PAP, May 2021)

The PAP site (49°N, 16.5°W) is a highly advective environment dominated by eddies which can cause upper ocean biogeochemical properties to evolve on time and space scales comparable to those driven by biological processes. The NA operations were conducted in a coherent, anticyclonic, physically retentive eddy that minimized horizontal exchanges, so that changes in biological or chemical properties were dominated by local rather than advective processes. An overview of the NA is available by Johnson et al. (2024). In short, the expedition sampled a dual-phase spring bloom with a transition to high sinking particle export. Conditions differed across the three sampled epochs. The first epoch (E1; May 5-7) was marked by a very large diatom biomass in the surface ocean but no presence of aggregates in the upper mesopelagic portion of the water column (Siegel et al., 2024). The second epoch (E2; May 11-20) followed a major storm (>40 kts) and was marked by a large change in surface properties and the appearance of aggregates. Export flux metrics remained low by most measures until the third epoch (E3; May 21-29) which large increases in both sinking particle fluxes and aggregate abundances (see e.g., Brzezinski et al., 2024; Clevenger et al., 2024; Meyer et al., 2024; Romanelli et al., 2024).

2.2 Platforms and instrumentation

The deployments during the NP expedition included coordinated sampling with two research vessels: a Process Ship (*R/V Roger Revelle*, cruise *RR1813*) focused on sampling biogeochemical stocks and fluxes, ecological abundances and rates, and optical properties following a Lagrangian float, and a Survey Ship (*R/V Sally Ride*, cruise *SR1812*) that characterized the horizontal and vertical distribution of properties including phytoplankton, particulate and dissolved organic carbon, ^{234}Th deficit, and other constituents surrounding the Process Ship and cross-calibrated sensors onboard the ships and the autonomous platforms (Siegel et al., 2021).

In the NA, a third ship was added to the Survey Ship (*RSS Discovery*, cruise *DY131*) and the Process Ship (*R/V James Cook*, cruise *JC214*), the *R/V Sarmiento de Gamboa* (cruise *SdG2105*),

that focused on plankton and metazoan imaging. Similar to the NP sensor calibration exercise, a detailed intercalibration was performed on all the NA sensor observations (Siegel et al., 2023). A summary of the instruments and measurements most relevant to this study is presented below.

2.2.1 Sediment trap fluxes

Two types of sediment traps with identical collection tubes (collection area = 0.0226 m^2) were used - neutrally buoyant sediment traps (NBSTs) and a surface-tethered sediment trap array (STT). Sinking particles were collected over approximately 2 to 5-day deployments in the upper 500 m of the ocean during the three epochs in each EXPORTS field campaign (Estapa et al., 2021; Johnson et al., 2024). Results from these traps are discussed here without distinction of trap type. Formalin-poisoned brine traps were gravity filtered through 335-micron screens, swimmers were manually removed from the screens under magnification, and the remaining material was recombined with < 335 μm material for bulk elemental analysis for POC. During the NP, sample composition was used to perform an additional correction for POC from small swimmers that could not be removed following screening (Estapa et al., 2021). POC fluxes were modest during E1 and E2, and increased moderately during E3. During NA, particle export flux seen in the traps increased rapidly two weeks after the experiment started, from similarly low fluxes in E1 and E2 to high fluxes in E3, suggesting strong temporal variability in flux (Siegel et al., 2024).

2.2.2 ^{234}Th fluxes

^{234}Th disequilibrium relative to Uranium-238 (^{238}U) in depths ranging from 0 to 500 m was used during EXPORTS to estimate POC fluxes following the methodological approach proposed by Buesseler et al. (1992). A description of the sampling method can be found in Clevenger et al. (2021). A full description of ^{234}Th measurements and derived fluxes from the NP experiment can be found in Buesseler et al. (2020), while the NA experiment is described in Clevenger et al., 2024. During the NP, the ^{234}Th data show relatively homogenous and consistent ^{234}Th disequilibria, with higher ^{234}Th fluxes observed at depths of 50 to 100 m, remaining relatively constant or decreasing at greater depths in the water column (see Figure 1 in Buesseler et al. (2020)). ^{234}Th-derived POC fluxes showed a similar trend, but with fluxes decreasing more sharply with increasing depth during all epochs. During NA, the magnitude of ^{234}Th disequilibria varied both temporally and spatially through the cruise. Existing deficits indicated that particle fluxes had already been high prior to the start of the cruise (Clevenger et al., 2024). Since ^{234}Th measurements are integrated

over time rather than an instantaneous representation of a system, a non-steady state model was needed to derive POC fluxes that increased during the experiment.

2.2.3 UVPs

The 5th generation of underwater cameras (UVP5; Picheral et al. 2010) was used to collect all PSD data used here. A total of 387 high-resolution full depth particle size spectra (0.10 – 26 mm equivalent spherical diameter, ESD) were sampled with five different UVPs mounted on the bottom of each ship CTD-Rosette. The smallest consistently sampled bin across all UVPs is centered at 0.14 mm while the largest size sampled is a function of particle concentrations. Details of these units and data provided by each are summarized in the Supporting Information (SI) and in the EXPORTS UVP intercalibration report by Siegel et al. (2023). A full description of the UVP5 can be found in Picheral et al. (2010) and a thorough review of the instrument, data collection, processing and quality control can be found in Kiko et al. (2022).

Briefly, the UVP5 acquires and processes images in real time using two lighting units, each consisting of a row of red-light emitting diodes (LEDs), that illuminate and images a well-defined volume of water of ~1L sample volume with 100 µm flashes of collimated light at a maximum rate of approximately 6 Hz (Picheral et al., 2010). Particles (living and non-living) are identified from each image and then sized as the number of contingent pixels. The projected area for each particle is then converted to equivalent spherical diameter (ESD). Particles are binned into size bins and the particle size spectra, *N(D)*, is determined as the number of particles in each size bin divided by the width of the bin. Data are acquired on the downcast of each CTD profile (drop rate ~1 m s^{-1}) and images are binned into 5-m depth intervals (with ~ 100 UVP scans per 5-m bin). Consequently, each depth bin represents a sampling volume of about 100 L. Further, PSD data from each platform were inter-calibrated to ensure comparability of data from different UVP units, as detailed in the EXPORTS UVP intercalibration report by Siegel et al. (2023) and summarized in the SI.

2.3 UVP-based POC flux estimates

Both the classic and our modified UVP-based POC flux estimates apply Eq. (2) to the PSD observations by optimizing the A and B coefficients using independent POC flux estimates from traps alone (classic UVP method) or both traps and ^{234}Th (our modified UVP method). Several considerations arise concerning how data are used to fit coefficients A and B, including the UVP

size range selected for fitting, the spatial area considered, vertical resolution of each technique, and temporal variability between epochs.

Particle size range considerations - UVPs have evolved over the years, with each model iteration expanding the size spectra measured (Picheral et al., 2022). In Guidi et al. (2008), data from older UVP models (UVPs 2, 3, and 4), resulted in an overlapping size range from 0.25 to 1.5 mm across 8 size bins (see Tables 2 and 3 in Guidi et al. (2008) for details). However, the UVP5 model covers a wider size range from 128 µm to 26 mm across 23 size bins (Picheral et al., 2022). To reproduce the classic UVP method used by Guidi et al. (2008) with a more recent instrument model two options were considered: the classic 8 size bins (250 µm to 1.5 mm) from Guidi et al. (2008) and an extended version using 23 size bins (128 µm to 26 mm). In both cases, we include all living and non-living particles as was done in Guidi et al. (2008).

Creating global and regional models - Guidi et al. (2008) established a global relationship between UVP-observed PSD and particle flux using UVP data from multiple locations and sediment trap fluxes that were not co-located in space or time (see Table 1 and Figure S1). To more closely replicate fitting at these larger global scales, we first reproduce a similar fit by calibrating our UVP data against POC fluxes observations from the combined EXPORTS data set. Note that unlike Guidi et al. (2008), the UVP data and POC observations are from the same time and study area. We refer to this as a "global" approach. We also used a "regional" comparison by fitting A and B considering UVP and flux data separately for the NP and the NA regions. Both approaches can be evaluated using either the 8 or newer 23 size bin criteria.

Sediment trap considerations - For the consideration of the spatial scales for the NP traps, we only matched UVP profiles and trap fluxes from the same source funnel, as described in Estapa et al. (2021). In essence, choosing only UVP profiles falling within the particle source region defined by local currents and assuming a particle sinking rate of 100 md^{-1} (e.g., Siegel et al. 2008). In the NA, the spatial criterion was related to the dimensions of the core of a retentive eddy that was sampled during the experiment in a Lagrangian fashion. In this case, only UVP profiles and trap flux within the eddy center (EC) waters (Johnson et al., 2024), defined as < 15 km from the autonomous asset-defined eddy center, were used.

Thorium-234 flux considerations - As both UVP images and ^{234}Th samples were collected on the same CTD cast, we could combine all of the paired UVP and ^{234}Th results on a cast-by-cast basis

for a global estimate of A and B using the NP and the NA results. Alternatively, these could be considered separately, to derive regional coefficients for the NP and the NA. Note there was little spatial variability in the NP, and all casts were included. However, for the NA, we restricted the ^{234}Th and UVP matchups to the eddy center, consistent with the approach used for the trap data.

Vertical Resolution Considerations - The three data sets used all have different vertical resolutions in their sampling. For comparisons to a specific trap depth, we used the average of the 5-m resolution UVP data at the measurement depth and the three 5-m depth intervals above it. This resulted in a 20-m depth average, corresponding to imaging roughly 400 L of seawater. See Table 1 for the resulting number of UVP profiles and sediment traps used in these global and regional comparisons.

In the case of ^{234}Th, we again matched the UVP data by averaging the 5-m intervals containing the ^{234}Th measurement and the three intervals above, similar to the traps. No ^{234}Th data in the mixed layer were used. See Table 1 for the resulting number of UVP and ^{234}Th profiles used in these global and regional comparisons.

Temporal variability between epochs - In the NP experiment, variability between epochs was considered minimal (Siegel et al., 2021). In the NA experiment, we clearly sampled the development of the evolving system (Johnson et al., 2024; Romanelli et al. 2024). At both sites, results from UVP, traps and ^{234}Th were grouped and averaged by epoch for comparison to the cruise average. The number of casts broken down by these epochs is found in Table S1.

3 Results

3.1 PSD observations

UVP-PSDs observations of in situ particles (# L^{-1} mm^{-1}) as a function of ESD (mm) binned in 5-m depth intervals are shown in Figure 1. In the NP, UVP-PSD observations exhibit little discernible temporal variations (Figure 1a and S2a). Conversely, in the NA, the PSDs changed throughout the cruise (Figure 1b, 1c, and S2b).

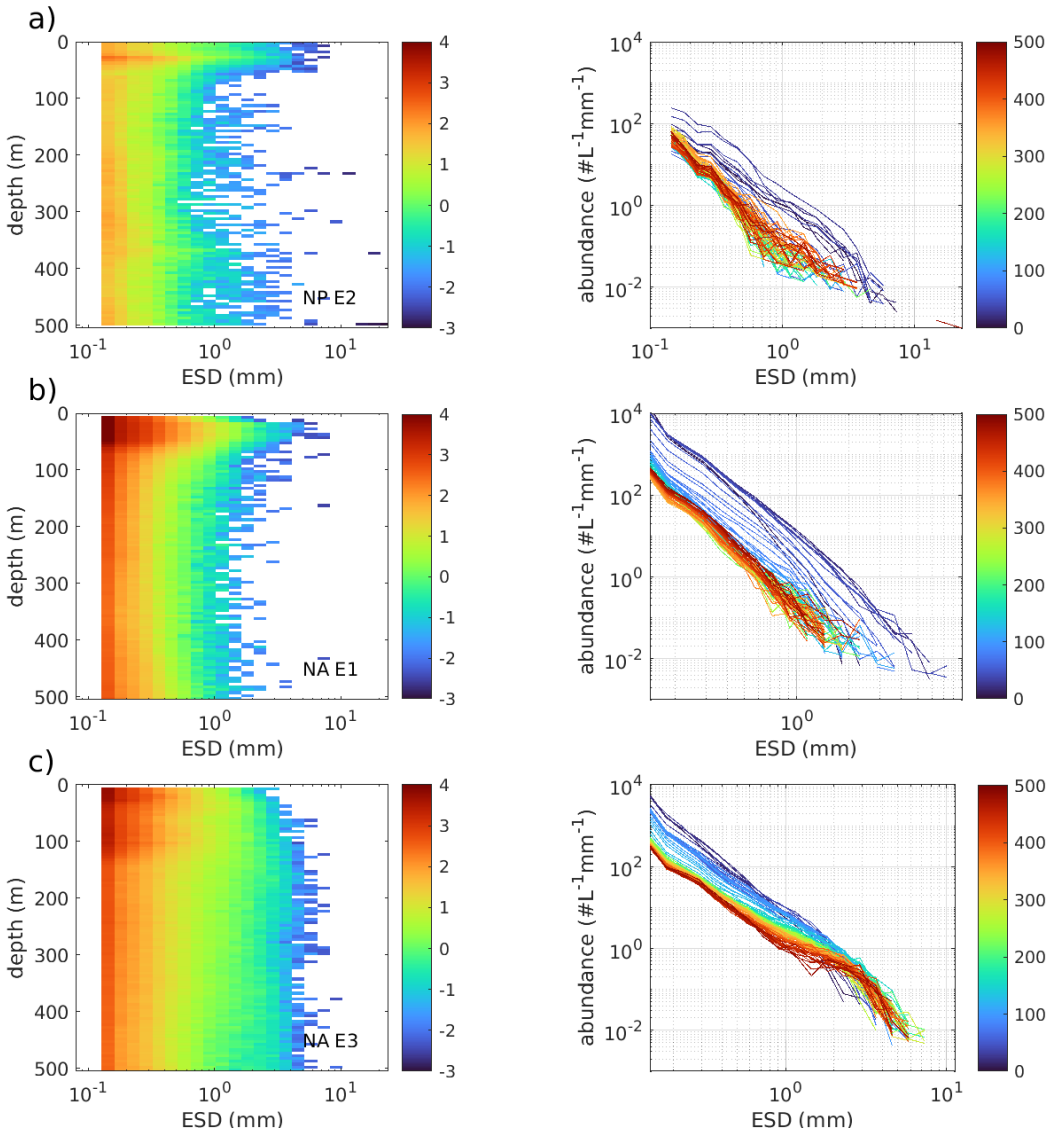

316

317 **Figure 1.** Observed particle size distribution (PSD) between epochs of in situ particles plotted against aggregate
318 equivalent spherical diameter (ESD, mm) for the a) NP and b-c) NA. For each panel, the figure on the left shows ESD
319 versus depth, the color bar indicates particle abundance for each size (in # L^{-1} mm^{-1}, logarithmic scale). Red indicates
320 a higher number of particles than blue. The figure on the right shows ESD versus abundance, the color bar indicates
321 depth (m). Red indicates deeper waters than blue. For the NP, no changes in PSD were observed over time and a
322 random profile in E2 was chosen. For the NA, PSD evolved between epochs and representative profiles early (E1)
323 and late (E3) in the cruise are shown.

324 As expected, PSDs decline in particle abundance with increasing size across all casts in both
325 experiments, with smaller particles being more abundant than large ones by several orders of
326 magnitude at all depths (see left panel in the figures). However, distinct vertical patterns emerge
327 for each experiment based on the particle size.

In the NP, abundances of small particles remain relatively consistent across depths and time, whereas larger particles decreased in abundance with depth and were constant at lower abundances below 100 m (see right panel in Figure 1a). In the NA, PSDs changed both over time and depth (see Figure 1b and 1c). During the initial days of the experiment (E1), small particles were highly concentrated in the surface layer (0-50 m) and decreased with depth, while deeper layers showed a shift toward fewer, larger particles. In the later stages of the experiment (E3), there was a substantial increase in large particles, especially at greater depth.

3.2 A and B coefficients using EXPORTS results

Table 1 displays present and prior estimates of A and B coefficients. Uncertainty bounds were calculated as the half-width of the interval of the obtained values and the confidence intervals (CIs) were provided as the range between their minimum and maximum values. The coefficient of determination for the linear fit (r^2) is also included, calculated as 1-(SSE/SS), where SSE is the sum of squared errors (differences between predicted and actual values), and SS is the total sum of square values (difference between actual values and their mean).

When applying the global approach using traps, i.e. calibrating all data from both sites for a single A and B value, no significant differences were observed within the uncertainty bounds in the retrieved A and B coefficients using either the 8-size bins or 23-size bins (Table 1). However, the ratio of uncertainty to estimate is > 1 for the 8 bins (SI, Figure S3). Hence, we only consider the full 23 size bins in our comparisons below (A = 13.1 ± 5.5 mg C d^{-1} mm^{1-b}, B = 1.54 ± 0.44, r^2 = 0.81, Figure 2a). The same global approach applied to ^{234}Th POC flux determinations is a poorer fit with a larger value of A though a similar B (A = 20.1 ± 2.9 mg C d^{-1} mm^{1-b}, B = 1.42 ± 0.15, r^2 = 0.56; Figure 2b). When applying the regional approach using traps, no significant differences were observed within the uncertainty bounds of the A and B coefficients compared to the global approach in the NA. However, there was no predictive power in the NP regional models. In contrast, when using ^{234}Th, there was no regional predictive capability in either of the deployments (Table 1).

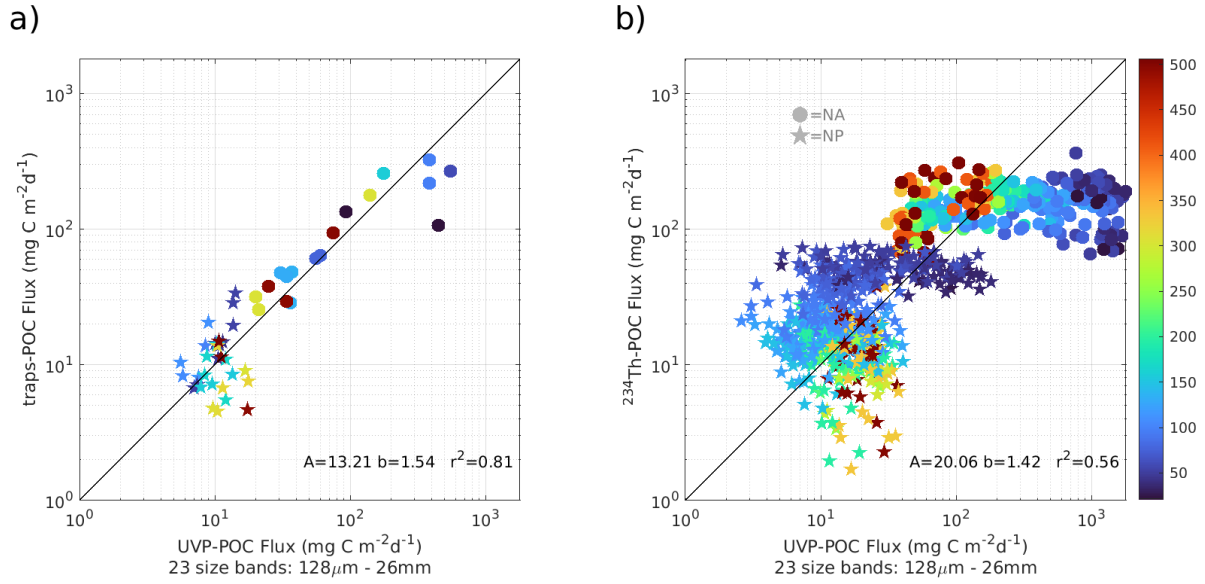

Figure 2. Results of the matchups between UVP-based POC fluxes (in mg C m^{-2} d^{-1}, x-axis) using a) traps and b) ^{234}Th (y-axis) using the global approach. Indicated in each panel along with the r^2 of the linear fit. 95% CIs for the A and B coefficients are provided in Table 1. Stars represent the NP results, and circles the NA results, with color representing depth (in m). The black line indicates the 1:1 line.

3.3 Vertical profiles of POC flux

Using the A and B values from EXPORTS, we can derive vertical profiles of POC flux from any given UVP profile in that study (Table 1). Figures 3 and 4 show the variability in UVP derived flux profiles for both the global (panels a and e) and regional (panels b-d and f-h) fit parameters for the NP and NA, respectively. Concurrent trap and ^{234}Th flux profile observations are overlain in the upper and lower rows of Figures 3 and 4, respectively. In each case, the flux profiles using UVP data show both extreme vertical variability and large cast to cast variability (gray lines).

For the NP, UVP fluxes range from 5 to 50 mg m^2 d^{-1} (global calibration against all traps; Figure 3a), with an average around 50 mg m^2 d^{-1} below the mixed layer depth (MLD) decreasing to vertically uniform values of ~ 10 mg m^2 d^{-1} below 100 m. Note however individual UVP casts even in the upper 50-100 m can have lower or higher fluxes predicted than these averages. The fit of the UVP average with the observational trap results in the NP is good within the spread of the trap data (Figure 3a). Similar patterns are found for the UVP fluxes calibrated with the ^{234}Th observations, although the fluxes are > 1.5 times higher, reflecting the higher values of A used (Figure 3d).

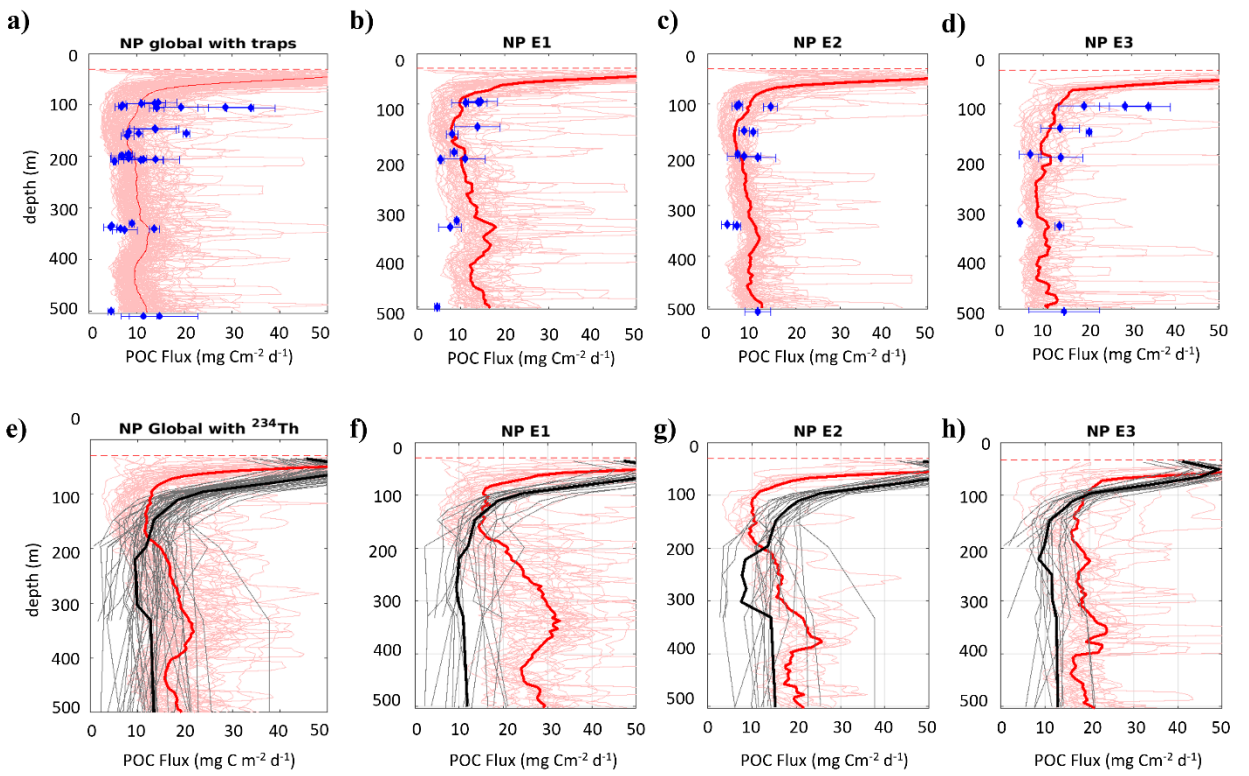

Figure 3. Vertical profiles of POC fluxes for (a) the global and (b-d) regional approaches in the NP using traps grouped by epochs: E1, E2, and E3 (from left to right) where the blue diamonds denote sediment trap POC fluxes with uncertainties from Estapa et al., (2021). Panels (e-h) show the corresponding UVP fluxes optimized using ^{234}Th data while the gray lines show the ^{234}Th-derived POC flux and the fluxes for each cast, and the black lines show the mean flux. The horizontal dashed line indicates the mean mixed layer depth over the course of the experiment. Pink lines show the UVP-based POC flux for each UVP cast, calculated using the A and B coefficients derived from each approach. Only UVP casts paired with trap or ^{234}Th profiles that fall within an epoch are shown. In panels (a) and (e) the red line represents the cruise mean UVP-based POC flux of all casts used for the fitting, which includes casts within a 100 md^{-1} source funnel region (see main text for details). In the rest of the panels, the red line indicates the epoch mean.

In principle, a regional calibration of A and B and concurrent UVP and flux observations might be expected to improve the matchups; however, that is not the case. Using regionally derived A and B for the NP with UVP derived flux profiles separated by epoch (Figures 3b-d), the UVP POC flux exceeds the traps around 350 m in E1 and E2 (Figures 3b and 3c), and the increase in trap flux in E3 at 100 m is not captured in the E3 UVP profiles (Figure 3d). Small scale changes in flux versus depth or time are thus not improved by using a regional fit to the NP trap data. Considering the NP regional model derived from ^{234}Th, individual ^{234}Th flux profiles vary cast to cast, but not

over as wide a range as the UVP derived fluxes (Figures 3f-h). A decrease in flux versus depth is seen in both UVP and ^{234}Th results, but with the UVP showing higher values on average at deeper depths (Figure 3e). A subsurface peak at a depth of ~350 m is observed in the ^{234}Th optimized UVP fluxes for all three epochs and is especially strong in the NP E1 (Figure 3f). Also, while ^{234}Th fluxes generally increase to some maximum value in the subsurface (here 50 m) and then decrease, UVP derived fluxes always are highest in the shallowest depths.

When we examine these same depth trends in the NA, the trap fluxes reach a maximum of > 500 mg m^2 d^{-1} for UVP derived fluxes using our global fit for the traps (Figure 4a). The magnitude and range of the UVP fluxes are considerably higher than in the NP. As noted previously, the progression of the bloom resulted in large local changes in particle properties, and this is illustrated clearly when the NA results are displayed by epoch. Using a NA regional calibration of the UVP data with traps, there is a better fit between UVP fluxes and traps if broken down by epoch, for which the flux values increase dramatically in E3, especially at depths > 100 m (Figures 4e versus Figures 4c and 4d).

The global fit using ^{234}Th data in the NA results in higher UVP fluxes on average (Figure 4e) and a predicted increase in flux using matched UVP profiles and regional fit in E3 (Figure 4, panels f-h). However, the shape of the two flux curves differs, with a higher flux at the surface and steeper flux attenuation evident in the UVP data but not in ^{234}Th results.

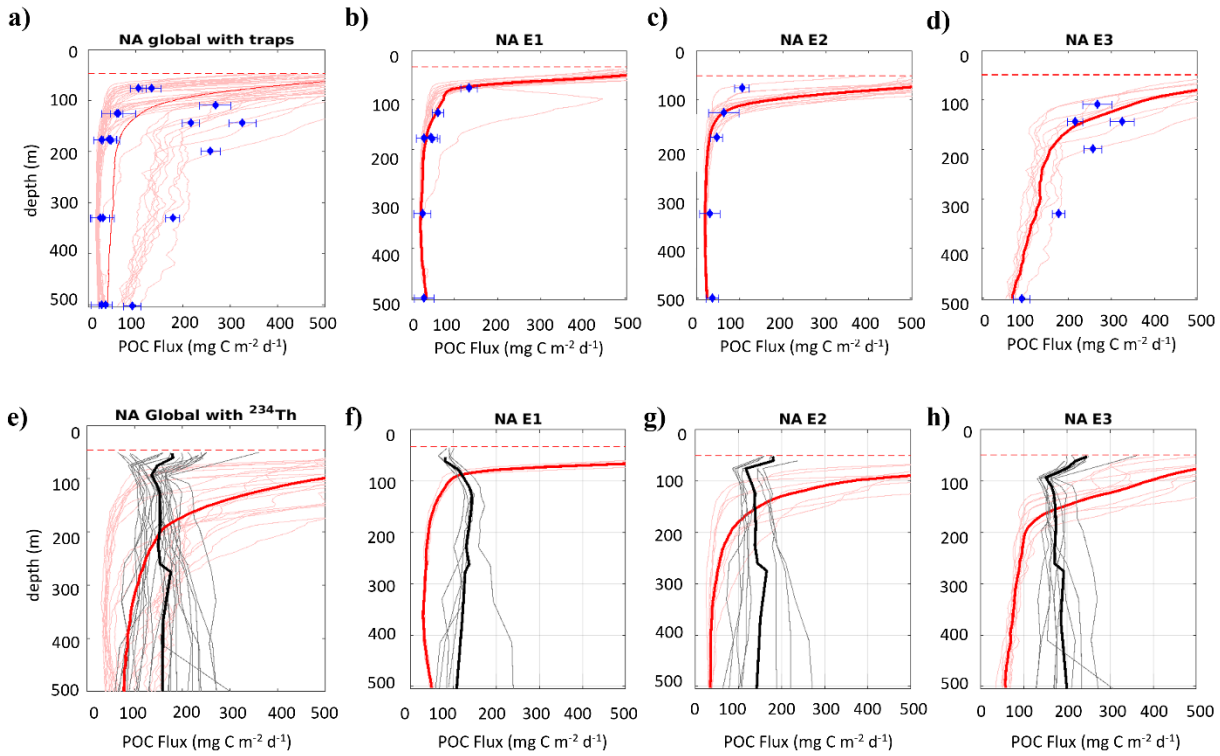

410

411 **Figure 4.** Corresponding figure to Figure 3 for the NA deployment. Casts used for the fitting include only those within
412 the eddy center.

413 ## 4 Discussion

414 We set out to assess the quality of POC flux estimates derived from the UVP imagery using
415 concurrent sediment traps and ^{234}Th flux observations. The challenges are substantial given the
416 multitude of issues presented. First, UVP images and the PSD derived from them, are at best
417 measures of sinking and non-sinking particles and living stocks, within certain size ranges and
418 over scales set by the number of images (Hz), imaging volume (liters) and duration of a CTD cast
419 (hours; meters) (Picheral et al., 2022). Traps measure the gravitational sinking flux of particles,
420 largely non-living, and originating from a large particle source area (Siegel et al., 2008) determined
421 by sinking rates, currents and deployment durations (several days; 10's km^2). Biases in trap fluxes
422 occur due to hydrodynamics, swimmers, preservation and other issues (Buesseler et al., 2007). The
423 ^{234}Th flux method tracks small scale variations in flux (km) but averaged over days to weeks. The
424 ^{234}Th-derived POC flux also depends on the measured ^{234}Th disequilibrium and generally ignore
425 physical processes, but importantly here, the flux can be sensitive to whether a system is at steady
426 state or not, over the course of its half-life (24.1 d) (Ceballos-Romero et al., 2018; Clevenger et

al., 2024; Savoye et al., 2006). A conversion from ^{234}Th flux to POC flux requires consideration of observed variations in its ratio to POC on particles that vary with depth and location (Buesseler et al., 2006). So, mismatches between UVP, trap and ^{234}Th estimates of POC flux are expected to be due to a combination of methodological consideration and their respective spatial and temporal averaging.

The EXPORTS project provides a unique opportunity to evaluate the utility of UVP-derived flux estimates using an extensive set of co-located and simultaneous sediment traps and ^{234}Th observations. A key finding is that UVPs can be effectively trained to translate observed PSD changes into POC fluxes when the range in POC fluxes spans several orders of magnitude, and when stocks and fluxes are roughly near steady state. At its most basic, and when in steady state, if there are more particles observed with the UVP, there is higher flux, and vice versa. In terms of flux attenuation versus depth, note that both POC stocks and POC fluxes decrease with depth (Lam & Bishop, 2007; Martin et al., 1987). However, when POC flux variations are smaller than an order of magnitude, i.e., at local scales, or are in non-steady state conditions, UVP approaches to determine flux have large uncertainties, and particle stocks are not necessarily a reflection on in-situ export. Here, we delve into the findings that led us to these insights.

4.1 Global performance of the modified UVP method

The globally optimized A and B coefficients found using traps and ^{234}Th fluxes range from 13.2 to 20.1 for A, and from 0.73 to 1.54 for B, respectively (8 and 23 size bins, Table 1). The other global estimates from Clements et al. (2023); Guidi et al. (2008); and Kriest (2002) range from 12.5 to 18.0 for A, and 2.2 to 3.8 for B (Table 1). All of these have considerable uncertainty, in particular our estimate using only 8 size bins.

Importantly, even small discrepancies in the A and B coefficients lead to significant differences in POC fluxes predicted from UVP data (Figure 5). These differences are primarily driven by the B coefficient, which is more sensitive to the particle size range than the A coefficient. Using the classic UVP-based POC flux coefficients for A and B, it would consistently underestimate trap-measured fluxes by about an order of magnitude, particularly at the lower flux ranges (Figure 5). Using regionally derived A's and B's would make these POC flux differences even larger, such as the regional estimates of A and B from the NP and the NA in EXPORTS, or using those from Iversen et al. (2010), Fender et al. (2019), or Forest et al. (2013), which focused on the Mauritanian

457 coast, the California Current Ecosystem, and the Southeast Beaufort Sea (Arctic Ocean),
458 respectively.

459 We attribute differences in the A and B coefficients primarily to differences in particle
460 characteristics found in the NP and during the spring bloom in the NA, compared to the prior
461 studies (SI, Figure S1). These differences are likely due to the different depth ranges considered
462 in each study, which is especially important since a single A and B values are applied at all depths.
463 Guidi et al. (2008) and Iversen et al. (2010) focused on deeper sinking aggregates (100–1000 m,
464 and 1200-1900 m depth respectively) than our study (0 -500 m depth). According to Guidi et al.
465 (2008), an increase in fractal dimension with depth implies a decrease in particle porosity, which
466 could account for their higher B values (3.8 and 4.3, respectively), as the physical compression of
467 aggregates due to fluid dynamics can compact them decrease porosity (Logan & Kilps, 1995). Our
468 EXPORTS results, which show lower B values (all values <1.6), suggest the presence of more
469 porous particles, likely aggregates, in the upper 500 m of the NP and NA.

470 We also consider whether changes in A and B reflect genuine variations in particle characteristics
471 rather than an artifact of the size range used by the imaging systems in different studies. Our 8 bin
472 size range was chosen to match Guidi et al. (2008), and yet the B in Guidi et al. (2008) is 5 times
473 higher (3.8 versus 0.7; Table 1). Therefore, we do not think size range is the primary reason here
474 for differences in A or B values, rather it is more likely to be attributed to differences in particle
475 properties.

476 Another aspect of UVP size ranges is that, at the smaller end, there can be an undercount of the
477 more abundant, but smallest sizes as one reaches the resolution limit of the UVP for identifiable
478 particles as these particles may not be detected or can be difficult to distinguish from background
479 noise (Stemmann & Boss, 2012). In this data set, there is no obvious tailing downward of PDS
480 slopes for the smaller sizes classes that would indicate this type of bias (Jackson et al., 1997). At
481 the larger size ranges, > 0.8 mm to 28 mm, the total particle counts drop off as there are very few
482 large particles in the ocean, and these typically decrease with depth. One reason we combine UVP
483 images from 5 m depth intervals is to increase imaging volume, and hence our chances of counting
484 more than one particle in these larger size bins. At an abundance of log 10^{-2} (Figure 1, y-axis), the
485 total number of particles counted would be less than 10 in our 100 L imaging volume for the size
486 bins from 0.8 mm and larger (Figure 1a). This difficulty in quantifying rare large particles, leads

to a high uncertainty that translates directly into large POC flux variability with depth, and between casts.

Another consideration is that if more data are from shallow waters, we would image a higher fraction of living versus non-living particles. Shallow water particles would be larger and more POC rich and include more non-sinking materials. Including living organisms detected by the UVP introduces uncertainty into flux calculations based on unsorted PSD data (Bisson et al., 2022). Supporting this, Kiko et al. (2020) found that excluding living organisms and artifacts larger than 1 mm ESD from the UVP5 dataset decreased the variability of PSD-derived POC flux estimates. Clearly, while one may desire to use UVPs to estimate fluxes for shallow depths, one needs to be careful of our calibration of UVPs. In EXPORTS, we only consider UVP flux estimates below the MLD and match the calibration data as closely as possible to the same depths as the flux observations.

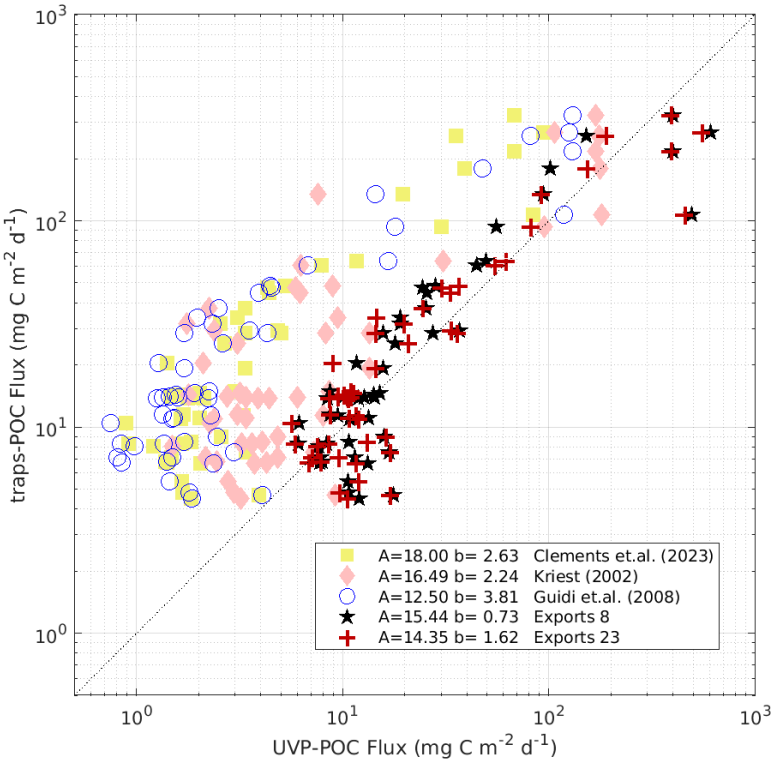

Figure 5. Results of the matchups between UVP-based POC fluxes (in mg m^{-2} d^{-1}, x-axis) and sediment trap fluxes (y-axis) using five different sets of A and B coefficients from previous studies and our own, applied to the entire EXPORTS data set. The coefficients used are from: 1) Clements et al. (2023) (yellow squares), 2) Kriest (2002)

(orange diamond), 3) Guidi et al. (2008) (blue circles), and the coefficients obtained in our study for the global approach using traps with 4) the same 8 size bins as used by Guidi et al. (2008) (black stars), and 5) 23 size bins (red cruxes; See Table 1).

4.2 Using traps versus ^{234}Th for calibration if UVP fluxes

The ^{234}Th approach has the advantage of being relatively easier to measure and at higher resolutions than traps; however, the cast by cast comparisons with UVP had low predictive power (Figure 2a and 2b; Table 1). Thorium-234 also has the advantage of providing flux data at shallower depths than sediment traps, the shallowest of which were deployed at 100 m in the NP experiment and 75 m in the NA experiment. The differences in the depth range covered by each technique likely contributes to the variations in A and B coefficients, resulting in a larger coefficient A for ^{234}Th than traps (20.1 versus 13.2 in global approach), which could reflect the higher number of shallow water particles considered when using UVP and ^{234}Th matchups. Since the gradients in POC flux are largest below the MLD and level off around 75 – 100 m in EXPORTS, the calibrations of A and B against UVP data necessitates tracers like ^{234}Th if we want to estimate flux at these shallower depths. Most importantly, a significant difference is that the temporal and spatial scales of integration differ for POC flux derived from traps versus ^{234}Th. Specifically, traps in EXPORTS have a shorter average time scale of flux over 3-4 days, but they involve larger spatial averaging over 10's of kilometers for the particle source regions (Siegel et al., 2008).

4.3 Regional performance of the modified UVP method

Our assumption in creating the regional UVP flux models was that there would be regional differences that influence how POC content and sinking speed relate to particle size, requiring distinct A and B coefficients for PSD-flux conversions. However, optimizing the A and B parameters to regional data sets led to higher uncertainty in UVP-based POC fluxes (Table 1). This means that while the "modified UVP method" can still be used for regional applications, high uncertainties are to be expected when flux variations used to calibrate the UVP are small, and results should be interpreted carefully. For instance, we attribute the lack of predictive power in the regional calibration in the NP - regardless of whether traps or ^{234}Th are used - to the minimal spatial and temporal variations in POC flux during the experiment. In the NA we see a higher range and variation in POC flux, which improved the flux calibrations using UVP and traps (Table 1). In sum, we consider UVPs well-suited for understanding large scale POC flux differences

across multiple orders of magnitude, as exemplified by studies like e.g., Clements et al. (2023). However, UVPs are less effective at refining small-scale or short-term export rates, especially if strong flux variations do not occur locally or temporally.

4.4 POC fluxes versus depth in the NP and NA

4.4.1 Insights from the NP profiles

The UVP fluxes, using either the global or regional models that were optimized using either the trap or 234Th fluxes or, performed poorly for the NP (Table 1). Temporal changes in export during the NP deployment were minimal, and the system exhibited largely steady state conditions in water mass properties, production rates, chlorophyll, particle stocks (McNair et al., 2023; Siegel et al., 2021) and UVP PSD profiles (Figures 1 and S2). Both trap and ^{234}Th results show no noteworthy changes in POC flux between E1 and E2, with only small increases detected by traps in E3 (Buesseler et al., 2020; Estapa et al., 2021). Figure 3b, 3c, 3d). Furthermore, the trap and ^{234}Th results were similar (Estapa et al., 2021); Figure 3), suggesting that over the study area, conditions were relatively constant with respect to POC flux, at least in the upper 500 m.

We do know, however, that sinking particle types vary with depth – from larger organic aggregates and fecal pellets at shallower depths to smaller aggregates and less labile particles as depth increases - and across the three deployment periods (Durkin et al., 2021). These depth-related changes in particle types suggest that depth-constant coefficients A and B may not fully account for differences in shallow, mid, and deeper mesopelagic particles observed in the UVP-based POC flux profiles (see Figures 3b, 3c, 3d). Different size-to-carbon and size-to-sinking-speed relationships (i.e., distinct A and B coefficients) at varying depths, or depth-dependent A and B relationships may be required to improve upon such UVP based assessments. Numerous particle features, such as gray level, circularity, skewness, or kurtosis among others, measured by UVPs, are currently underutilized but could be valuable for capturing depth-related particle changes (Karthäuser et al., *in review*). We recommend further investigation into these parameters to improve the accuracy of UVP-based POC flux profiles in future studies.

Other studies from EXPORTS in the NP indicate that POC available for export out of the MLD primarily exists in the form of small particles driven by mesozooplankton repackaging of biomass or detritus (Durkin et al., 2021; McNair et al., 2023), as larger marine snow aggregates (particles > 0.5 mm) were not detected in Marine Snow Catcher deployments between 20-500 m (Romanelli

et al., 2024). Durkin et al. (2021) used sediment traps equipped with polyacrylamide gel layers to assess the contribution of small particles (< 100 µm) to total POC flux. They found that during the NP, small particles contributed 7% to 36% (mean contribution of 17% ± 9%) of total POC flux at depths between 95 and 510 m. However, Estapa et al. (2021) concluded that traps undercollected small particles due to hydrodynamic effects (Buesseler et al., 2007). Thus, the contribution of particles smaller than the UVP lower detection limit may have been higher than 17%. Ultimately, flux calculated from UVPs is highly sensitive to small particles (Bisson et al., 2022). This could explain why discrepancies between UVP-based POC fluxes and observations are even larger for ^{234}Th, which should reflect the export of particles across all sizes (Buesseler et al., 2007).

Limitations in imaging at the larger limit of the UVP size range may also affect the interpretation of fluxes. Larger particles disproportionately influence the overall UVP-based POC flux due to their substantial volume and rapid sinking speeds. As particle volume scales by its diameter cubed, even a small number of large particles can significantly contribute to the total flux. For instance, in the NP, UVP-based POC flux estimates from particles larger than ~ 0.1 mm derive from fewer than ten particles imaged per 100 L (5-m bins) (Figure 1a, right panel). If we consider the average POC flux value at depths of 150 or 300 m, typically around 10 - 20 mg m^2 d^{-1}, just a few additional large particles can have a substantial impact on POC flux. For example, for particles in the 5 - 8 mm size bins, just ten particles would contribute between 10 to > 40% of the total POC flux when using the UVP method calibrated with traps. Because of differences in A and B, if the calibration is based on ^{234}Th, the contribution to flux of rare particles increases, accounting for 17% to 68% of the total POC flux. This issue is less relevant in the NA, where POC fluxes at 150 or 300 m range from 50 to 200 mg m2 d^{-1}. In the NA, particles > 1 mm would have contributed between 1% to 13% of the total flux, while only being counted in fewer than 10 images.

These results emphasize the importance of rare large particles in the NP are supported by observations related to salp fecal pellets, whose presence in small numbers in the NP has been shown to account for a significant portion of POC flux (Durkin et al., 2021; Steinberg et al., 2023). Missing such large particles in UVP imaging could lead to significant underestimation of POC flux, leading to misleading conclusions about carbon export dynamics. The sporadic presence of these large particles would also explain the fluctuating nature of UVP-derived POC flux profiles versus depth and the high cast-to-cast variability. Since large particles are infrequent but have a

disproportionately large impact on flux, their presence would lead to spikes in the flux data. Estapa et al. (2021) also extrapolated the PSD from gel traps to larger sizes (> 1 mm) and concluded that traps undercollected rare larger particles, including salp fecal pellets, which would make the trap POC flux results too low. The ^{234}Th distribution should reflect these rare salp pellets. However, the fact that ^{234}Th and trap fluxes largely agree in the NP suggests this is not a big issue. The largest difference in the POC flux profiles is from the overall larger A and B's from ^{234}Th, which we can attribute to sampling shallower in the water column, leading to higher POC fluxes at all depths.

In the NP during E1 (Figure 3f) there is a large peak between 300 - 400m in the UVP derived fluxes, which may indicate some active transport layer. Salps were observed migrating from between 300 to 750 m during the day to the upper 100 m at night, (Steinberg et al., 2023). Notably, during E1, salp fecal pellet export was highest, comprising 48.1%, 88%, 85%, and 57% of the modeled total POC flux at 100, 208, 336, and 500 m, respectively (Steinberg et al., 2023), coinciding with the largest discrepancies between UVPs and ^{234}Th and, to a lower extent, traps. Migrating zooplankton actively transporting carbon could bypass sediment traps and leave behind particles that are non-sinking (no increase in ^{234}Th flux at the same depths is seen) but could be reflected in the UVP data. We suggest future studies analyze UVP casts separated by day and night to further explore daily migrations in order to test this hypothesis.

4.4.2 Insights from the NA profiles

Discrepancies of UVP-based POC flux results relative to traps and ^{234}Th measurements in the NA experiment cannot be solely explained by depth variations in A and B. Instead, we attribute the variability in the different flux indicators to temporal factors (SI, Figure S4).

The NA cruise took place during a dual-phase spring bloom in a highly dynamic system (Johnson et al., 2024; Romanelli et al., 2024; Siegel et al., 2024). Briefly, during E1 (May 5-7, storm 1 on May 7-11), export fluxes were low across most measures, including sediment traps and ^{234}Th (Figure 4, upper and bottom panels respectively), and as estimated by the Marine Snow Catcher, which collect no aggregates (Romanelli et al., 2024). After storm 2 (May 15) in E2 (May 11-20), aggregates were collected in the Marine Snow Catchers, but export fluxes remained low until E3 (May 21-29), when large particles substantially increased, particularly at depth (see Figure 2a in (Siegel et al. 2024). Shifts in the dominant plankton community, from large diatoms to a more diverse phytoplankton community were observed later in E3 (San Soucie et al. *in review*).

Throughout the NA experiment, particles were consistently fluffy and porous, becoming progressively fluffier and more porous over time, with large particles exhibiting extreme porosity that increased as the cruise progressed (Siegel et al. 2024; Soucie et al. *in review*). Analysis of the morphology of individual large (≥ 1 mm) particles sampled in the images collected by the UVP showed that fluffy aggregates dominated the dataset, accounting for 88% of the particles, while dense aggregates (10%), fecal pellets (1%), and zooplankton pellets (1%) made up the rest (Drago, 2023).

Under these conditions, the average of the UVP profiles effectively captured the bloom stages, mirroring the trap results, both of which increase in E3 (Figures 4a-d). POC fluxes from traps varied by an order of magnitude between E1 and E3, which allowed us to effectively train UVPs to translate observed PSD changes into POC fluxes. We attribute the good agreement between techniques to the main particles contributing to flux falling within the UVP's detectable size range (i.e., no significant contribution of particles < 100 µm) and a low presence of rare large particles. This, together with consistently fluffy and porous particle morphologies with depth and time, led to accurate calibration of A and B coefficients.

However, the performance of the ^{234}Th-derived POC fluxes was poor for both the global and regional tuning (Figures 4e-h). Differences in between traps and ^{234}Th in the NA have previously been reported at the EXPORTS sampling site and were linked to the persistence of ^{234}Th disequilibrium in the water column prior to sampling (Ceballos-Romero et al., 2016, 2018). Clevenger et al. (2024) suggest that the ^{234}Th profiles during the EXPORTS cruise reflect both an earlier export in addition to the evolving conditions. We conclude that the prior export likely contribute to the differences observed in the UVP flux calibration between traps and ^{234}Th in the NA. We see this both in shallow and in deeper depths. The ^{234}Th deficit at depth indicates that export had reached deeper waters from the previous time-period. This explains the much higher ^{234}Th-derived POC fluxes compared to traps and UVPs at depth. The export from the first bloom also would influence the calibration of A and B coefficients using ^{234}Th, at the same time leading to the low predictive power for the regional NA ^{234}Th method. Fluxes based upon ^{234}Th do increase in E3 but are not reflected in the UVP particle fields that are responding more quickly. Therefore, in highly dynamic and non-steady state environments like the NA, changing ^{234}Th distributions to the evolving particle fields measured by UVPs.

The evolving particle characteristics also would have impacted the accuracy of UVP fluxes given that A and B coefficients were held constant across epochs. However, determining A and B coefficients for each epoch was not possible given the higher uncertainties that would result with even smaller data sets.

5 Conclusions

Our modified UVP method successfully reflects large-scale POC flux changes globally (i.e., NP versus NA) and temporally (i.e., early versus late stages of the bloom), but struggles with vertical and temporal changes at regional scales. We conclude that the limited predictive power of the regional approach in the NP with both traps and ^{234}Th is due to small changes in the magnitude of the POC flux observations used to calibrate UVP data, coupled with the disproportionate contribution of rare large particles to the flux. In the NA, the calibration using sediment traps had a higher predictive power than using ^{234}Th, better capturing the larger scales and changing conditions represented by both traps and UVP averages during each epoch. UVP flux calibrations using ^{234}Th were ineffective in the NA due to the influence of an earlier export event on ^{234}Th deficits, in addition to the cast-by-cast mismatch between changing particle stocks measured by UVPs, and flux determined with non-steady state ^{234}Th models. Further studies calibrating UVP against ^{234}Th are crucial to draw more definitive conclusions about the performance of the approach with ^{234}Th in non-steady-state conditions, as ^{234}Th can be applied at shallower depths and with higher vertical resolution. Exploring using UVPs to quantify changes in particle stocks over time versus the assumptions here that higher stocks reflect higher fluxes, would be informative.

The classic and modified UVP methods for estimating POC fluxes from UVP-based PSDs are valuable but face several challenges, including limitations in imaging size and resolution, and other methodological concerns. Technological advancements are needed to sample larger volumes and detect a broader range of particle sizes. Coefficients A and B, derived through minimization procedures, can introduce errors influenced by the particle size range, the depth range over which calibrations are possible, detection limits for imaging rare large particles, and the assumption of constant A and B versus location, depth, and time. Measurement uncertainties can exceed 50% for PSD-based POC flux estimates (Bisson et al., 2022). Variations in A and B used in different studies can result in order of magnitude differences in predicted POC flux (Figure 5).

Since the variability with depth and between casts in UVP data is large, UVP users should not rely on a few UVP profiles to calibrate their own A and B coefficients, regardless of whether co-located trap flux measurements are available. Ideally, users should fit A and B coefficients to a large number of UVP profiles and co-located flux estimates for more accurate results. However, when this is not feasible, for global applications in the upper 500 m, we recommend using the coefficients from the "global approach using traps from this study" from Table 1, as they were co-located in space and time. For regional applications in the upper 500 m in the NA, we recommend using the coefficients from the "regional approach using traps NA" (Table 1). In general, for regional applications, more co-located data from other regions and times are needed to assess the variability of the A and B coefficients and further refine them for improved regional and global applications.

Moving forward, we propose exploring alternative approaches that consider particle morphologies for more accurate UVP-based POC flux estimates. Relying on particle size alone neglects the importance of morphology, which is likely crucial for accurately assessing export variations over time and depth. Furthermore, the optical properties of particles, particularly their index of refraction, are linked to their carbon content, as demonstrated in phytoplankton (Stramski, 1999), and likely hold true for other types of particles such as zooplankton, detritus, etc. Incorporating these optical characteristics alongside morphology could enhance our understanding of particle composition and its role in carbon export. Unsorted PSD data only provides fluxes derived from consideration of standing stocks, which may or may not accurately reflect real POC fluxes. At a minimum, particles should be categorized as living and non-living, with ideally, a more detailed classification considering different particle types across the water column. We recommend further studies to compare UVP-based POC flux with estimates from gel traps and include morphological sorting of sinking particles, as introduced in Trudnowska et al., 2021. This combined approach could enhance the accuracy of UVP-based POC flux estimates, helping to distinguish between living and non-living particles, identify dominant morphological groups specific to each sampling site and time, and advance our comprehension of carbon export dynamics in marine environments.

Acknowledgments

This work was supported by NASA Ocean Biology and Biogeochemistry program, the National Science Foundation Biological and Chemical Oceanography programs and the Woods Hole Oceanographic Institution's Ocean Twilight Zone study. We greatly acknowledge the cooperation,

714 skill and commitment of the Captains, Crews, Research Technicians and Administrative Staffs of
715 the R/V Roger Revelle (RR1813), R/V Sally Ride (SR1812), RRS James Cook (JC214), RRS
716 Discovery (DY131) and the R/V Sarmiento de Gamboa (SdG2105). ECR acknowledges the
717 support of the "Ocean Twilight Zone" project at the Woods Hole Oceanographic Institution
718 through a Postdoctoral Scholarship. This project has received funding from the European Union's
719 Horizon 2020 research and innovation programme under the Marie Skłodowska-Curie grant
720 agreement No 101032903. RK acknowledges support via a "Make Our Planet Great Again" grant
721 of the French National Research Agency within the "Program d'Investissements d'Avenir";
722 reference "ANR-19MPGA-0012" and funding from the Heisenberg Programme of the German
723 Science Foundation #KI 1387/5-1.

724 **Availability Statement**

725 NASA-funded primary data products are archived at SeaWiFS Bio-optical Archive and Storage
726 System (SeaBASS). All EXPORTS data are being archived under one digital object identifier
727 (DOI: http://dx.doi.org/10.5067/SeaBASS/EXPORTS/DATA001) that further expands into the
728 individual data subsets. NSF-funded. To find out information about all the data collected during
729 the EXPORTS field campaigns, their data repositories and availability, please visit:
730 https://sites.google.com/view/oceanexports/home.

731 **References**

732 Alldredge, A. (1998). The carbon, nitrogen and mass content of marine snow as a function of
733 aggregate size. *Deep Sea Research Part I: Oceanographic Research Papers*, *45*(4–5), 529–
734 541. https://doi.org/10.1016/S0967-0637(97)00048-4

735 Alldredge, A. L., & Gotschalk, C. (1988). In situ settling behavior of marine snow. *Limnology*
736 *and Oceanography*, *33*(3), 339–351. https://doi.org/10.4319/lo.1988.33.3.0339

737 Bisson, K. M., Kiko, R., Siegel, D. A., Guidi, L., Picheral, M., Boss, E., & Cael, B. B. (2022).
738 Sampling uncertainties of particle size distributions and derived fluxes. *Limnology and*
739 *Oceanography: Methods*, 2022. https://doi.org/10.1002/lom3.10524

740 Boyd, P. W., & Trull, T. W. (2007). Understanding the export of biogenic particles in oceanic
741 waters: Is there consensus? *Progress in Oceanography*, *72*(4), 276–312.
742 https://doi.org/10.1016/j.pocean.2006.10.007

743 Boyd, Philip W., Claustre, H., Levy, M., Siegel, D. A., & Weber, T. (2019). Multi-faceted
744 particle pumps drive carbon sequestration in the ocean. *Nature*, *568*(7752), 327–335.
745 https://doi.org/10.1038/s41586-019-1098-2

746 Brzezinski, M. A., Johnson, L., Estapa, M., Clevenger, S., Roca-Martí, M., Romanelli, E., et al.
747 (2024). Physical Mechanisms Sustaining Silica Production Following the Demise of the
748 Diatom Phase of the North Atlantic Spring Phytoplankton Bloom During EXPORTS.
749 *Global Biogeochemical Cycles*, *38*(7), e2023GB008048.
750 https://doi.org/10.1029/2023GB008048

751 Buesseler, K. O., Benitez-Nelson, C. R., Moran, S. B., Burd, A., Charette, M., Cochran, J. K., et
752 al. (2006). An assessment of particulate organic carbon to thorium-234 ratios in the ocean
753 and their impact on the application of 234Th as a POC flux proxy. *Marine Chemistry*,
754 *100*(3-4 SPEC. ISS.), 213–233. https://doi.org/10.1016/j.marchem.2005.10.013

755 Buesseler, K. O., Trull, T. W., Steinberg, D. K., Silver, M. W., Siegel, D. A., Saitoh, S. I., et al.
756 (2008). VERTIGO (VERtical Transport In the Global Ocean): A study of particle sources
757 and flux attenuation in the North Pacific. *Deep-Sea Research Part II: Topical Studies in*
758 *Oceanography*, *55*(14–15), 1522–1539. https://doi.org/10.1016/j.dsr2.2008.04.024

759 Buesseler, Ken O., Bacon, M. P., Kirk Cochran, J., & Livingston, H. D. (1992). Carbon and
760 nitrogen export during the JGOFS North Atlantic Bloom experiment estimated from 234Th:
761 238U disequilibria. *Deep Sea Research Part A, Oceanographic Research Papers*, *39*(7–8),
762 1115–1137. https://doi.org/10.1016/0198-0149(92)90060-7

763 Buesseler, Ken O., Antia, A. N., Chen, M., Fowler, S. W., Gardner, W. D., Gustafsson, O., et al.
764 (2007). An assessment of the use of sediment traps for estimating upper ocean particle
765 fluxes. *Journal of Marine Research*, *65*(3), 345–416.
766 https://doi.org/10.1357/002224007781567621

767 Buesseler, Ken O., Benitez-Nelson, C. R., Roca-Martí, M., Wyatt, A. M., Resplandy, L.,
768 Clevenger, S. J., et al. (2020). High-resolution spatial and temporal measurements of
769 particulate organic carbon flux using thorium-234 in the northeast Pacific Ocean during the
770 EXport Processes in the Ocean from RemoTe Sensing field campaign. *Elementa: Science of*
771 *the Anthropocene*, *8*(1). https://doi.org/10.1525/elementa.030

Ceballos-Romero, E., Le Moigne, F. A. C., Henson, S., Marsay, C. M., Sanders, R. J., García-Tenorio, R., & Villa-Alfageme, M. (2016). Influence of bloom dynamics on Particle Export Efficiency in the North Atlantic: a comparative study of radioanalytical techniques and sediment traps. *Marine Chemistry*, *186*, 198–210. https://doi.org/10.1016/j.marchem.2016.10.001

Ceballos-Romero, E., De Soto, F., Le Moigne, F. A. C., García-Tenorio, R., & Villa-Alfageme, M. (2018). 234 Th-Derived Particle Fluxes and Seasonal Variability: When Is the SS Assumption Reliable? Insights From a Novel Approach for Carbon Flux Simulation. *Geophysical Research Letters*, *45*(24), 13,414-13,426. https://doi.org/10.1029/2018GL079968

Clements, D. J., Yang, S., Weber, T., McDonnell, A. M. P., Kiko, R., Stemmann, L., & Bianchi, D. (2023). New Estimate of Organic Carbon Export From Optical Measurements Reveals the Role of Particle Size Distribution and Export Horizon. *Global Biogeochemical Cycles*, *37*(3), 1–21. https://doi.org/10.1029/2022GB007633

Clevenger, S. J., Benitez-Nelson, C. R., Drysdale, J., Pike, S., Puigcorbé, V., & Buesseler, K. O. (2021). Review of the analysis of 234Th in small volume (2–4 L) seawater samples: improvements and recommendations. *Journal of Radioanalytical and Nuclear Chemistry*, *329*(1). https://doi.org/10.1007/s10967-021-07772-2

Clevenger, S. J., Benitez-Nelson, C. R., Roca-Martí, M., Bam, W., Estapa, M., Kenyon, J. A., et al. (2024). Carbon and silica fluxes during a declining North Atlantic spring bloom as part of the EXPORTS program. *Marine Chemistry*, *258*, 104346. https://doi.org/10.1016/j.marchem.2023.104346

Davis, R. E., DeSzoeke, R., Halpern, D., & Niiler, P. (1981). Variability in the upper ocean during MILE. Part I: The heat and momentum balances. *Deep Sea Research Part A. Oceanographic Research Papers*, *28*(12), 1427–1451. https://doi.org/10.1016/0198-0149(81)90091-1

Drago, L. (2023). *Analyse globale de la pompe à carbone biologique à partir de données en imagerie quantitative*. Biodiversité et Ecologie. Sorbonne Université, 2023. Français. ⟨NNT : 2023SORUS562⟩. ⟨tel-04483392⟩

Durkin, C. A., Buesseler, K. O., Cetinić, I., Estapa, M. L., Kelly, R. P., & Omand, M. (2021). A Visual Tour of Carbon Export by Sinking Particles. *Global Biogeochemical Cycles*, *35*(10), 2021.02.16.431317. https://doi.org/10.1029/2021GB006985

Eppley, R. W., & Peterson, B. J. (1979). Particulate organic matter flux and planktonic new production in the deep ocean. *Nature*, *282*(5740), 677–680. https://doi.org/10.1038/282677a0

Erickson, Z. K., Fields, E., Johnson, L., Thompson, A. F., Lilian, A., Asaro, E. A. D., & Siegel, D. A. (2023). Eddy tracking from in situ and satellite observations. *ESS Open Archive*. https://doi.org/10.22541/essoar.167979672.22588418/v1

Estapa, M., Buesseler, K., Durkin, C. A., Omand, M., Benitez-Nelson, C. R., Roca-Martí, M., et al. (2021). Biogenic sinking particle fluxes and sediment trap collection efficiency at Ocean Station Papa. *Elementa*, *9*(1). https://doi.org/10.1525/elementa.2020.00122

Forest, A., Stemmann, L., Picheral, M., Burdorf, L., Robert, D., Fortier, L., & Babin, M. (2012). Size distribution of particles and zooplankton across the shelf-basin system in southeast Beaufort Sea: Combined results from an Underwater Vision Profiler and vertical net tows. *Biogeosciences*, *9*(4), 1301–1320. https://doi.org/10.5194/bg-9-1301-2012

Giering, S. L. C., Cavan, E. L., Basedow, S. L., Briggs, N., Burd, A. B., Darroch, L. J., et al. (2020). Sinking Organic Particles in the Ocean—Flux Estimates From in situ Optical Devices. *Frontiers in Marine Science*, *6*, 834. https://doi.org/10.3389/fmars.2019.00834

Guidi, L., Jackson, G. A., Stemmann, L., Miquel, J. C., Picheral, M., & Gorsky, G. (2008). Relationship between particle size distribution and flux in the mesopelagic zone. *Deep-Sea Research Part I: Oceanographic Research Papers*, *55*(10), 1364–1374. https://doi.org/10.1016/j.dsr.2008.05.014

Guidi, L., Stemmann, L., Jackson, G. A., Ibanez, F., Claustre, H., Legendre, L., et al. (2009). Effects of phytoplankton community on production, size, and export of large aggregates: A world-ocean analysis. *Limnology and Oceanography*, *54*(6), 1951–1963. https://doi.org/10.4319/lo.2009.54.6.1951

Guidi, L., Legendre, L., Reygondeau, G., Uitz, J., Stemmann, L., & Henson, S. A. (2015). A new

look at ocean carbon remineralization for estimating deepwater sequestration. *Global Biogeochemical Cycles*, *29*(7), 1044–1059. https://doi.org/10.1002/2014GB005063

Guidi, L., Chaffron, S., Bittner, L., Eveillard, D., Larhlimi, A., Roux, S., et al. (2016). Plankton networks driving carbon export in the oligotrophic ocean. *Nature*, *532*(7600), 465–470. https://doi.org/10.1038/nature16942

Henson, S. A., Sanders, R., Madsen, E., Morris, P. J., Le Moigne, F., & Quartly, G. D. (2011). A reduced estimate of the strength of the ocean's biological carbon pump. *Geophysical Research Letters*, *38*(4), n/a-n/a. https://doi.org/10.1029/2011GL046735

Honjo, S., Manganini, S. J., Krishfield, R. A., & Francois, R. (2008). Particulate organic carbon fluxes to the ocean interior and factors controlling the biological pump: A synthesis of global sediment trap programs since 1983. *Progress in Oceanography*, *76*(3), 217–285. https://doi.org/10.1016/j.pocean.2007.11.003

Iversen, M. H., Nowald, N., Ploug, H., Jackson, G. A., & Fischer, G. (2010). High resolution profiles of vertical particulate organic matter export off Cape Blanc, Mauritania: Degradation processes and ballasting effects. *Deep-Sea Research Part I: Oceanographic Research Papers*, *57*(6), 771–784. https://doi.org/10.1016/j.dsr.2010.03.007

Johnson, L., Siegel, D. A., Thompson, A. F., Fields, E., Erickson, Z. K., Cetinic, I., et al. (2024). Assessment of oceanographic conditions during the North Atlantic EXport processes in the ocean from RemoTe sensing (EXPORTS) field campaign. *Progress in Oceanography*, *220*, 103170. https://doi.org/10.1016/j.pocean.2023.103170

Karthäuser, C., Ceballos, E., Bam, W., Clevenger, S. J., Sievert, S. M., & Buesseler, K. O. (*in review*). Capturing individual marine particle properties that drive carbon flux. Science Advances.

Kiko, R., Biastoch, A., Brandt, P., Cravatte, S., Hauss, H., Hummels, R., et al. (2017). Biological and physical influences on marine snowfall at the equator. *Nature Geoscience*, *10*(11), 852–858. https://doi.org/10.1038/NGEO3042

Kiko, Rainer, Brandt, P., Christiansen, S., Faustmann, J., Kriest, I., Rodrigues, E., et al. (2020). Zooplankton-Mediated Fluxes in the Eastern Tropical North Atlantic. *Frontiers in Marine*

857 *Science*, *7*(May), 1–21. https://doi.org/10.3389/fmars.2020.00358

858 Kiko, Rainer, Picheral, M., Antoine, D., Babin, M., Berline, L., Biard, T., et al. (2022). A global
859 marine particle size distribution dataset obtained with the Underwater Vision Profiler 5
860 (Discussion). *Earth System Science Data Discussions*, *14*(9), 4315–4337.
861 https://doi.org/10.5194/essd-2022-51

862 Kriest, I. (2002). Different parameterizations of marine snow in a 1D-model and their influence
863 on representation of marine snow, nitrogen budget and sedimentation. *Deep Sea Research*
864 *Part I: Oceanographic Research Papers*, *49*(12), 2133–2162.
865 https://doi.org/10.1016/S0967-0637(02)00127-9

866 De La Rocha, C. L. (2007). The Biological Pump. In *Treatise on Geochemistry* (Vol. 6–9, pp. 1–
867 29). Elsevier. https://doi.org/10.1016/B0-08-043751-6/06107-7

868 Logan, B. E., & Kilps, J. R. (1995). Fractal dimensions of aggregates formed in different fluid
869 mechanical environments. *Water Research*, *29*(2), 443–453. https://doi.org/10.1016/0043-
870 1354(94)00186-B

871 Lombard, F., & Kiørboe, T. (2010). Marine snow originating from appendicularian houses: Age-
872 dependent settling characteristics. *Deep Sea Research Part I: Oceanographic Research*
873 *Papers*, *57*(10), 1304–1313. https://doi.org/10.1016/j.dsr.2010.06.008

874 Martin, J. H., Knauer, G. A., Karl, D. M., & Broenkow, W. W. (1987). VERTEX: carbon cycling
875 in the northeast Pacific. *Deep Sea Research Part A, Oceanographic Research Papers*,
876 *34*(2), 267–285. https://doi.org/10.1016/0198-0149(87)90086-0

877 McDonnell, A. M. P., & Buesseler, K. O. (2010). Variability in the average sinking velocity of
878 marine particles. *Limnology and Oceanography*, *55*(5), 2085–2096.
879 https://doi.org/10.4319/lo.2010.55.5.2085

880 McNair, H. M., Meyer, M. G., Lerch, S. J., Maas, A. E., Stephens, B. M., Fox, J., et al. (2023).
881 Quantitative analysis of food web dynamics in a low export ecosystem. *BioRxiv*,
882 2023.03.17.532807. https://doi.org/10.1101/2023.03.17.532807

883 Meyer, M. G., Brzezinski, M. A., Cohn, M. R., Kramer, S. J., Paul, N., Sharpe, G., et al. (2024).
884 Size-Fractionated Primary Production Dynamics During the Decline Phase of the North

Atlantic Spring Bloom. *Global Biogeochemical Cycles*, *38*(7), e2023GB008019. https://doi.org/10.1029/2023GB008019

Le Moigne, F. A. C., Villa-Alfageme, M., Sanders, R. J., Marsay, C., Henson, S., & García-Tenorio, R. (2013). Export of organic carbon and biominerals derived from 234Th and 210Po at the Porcupine Abyssal Plain. *Deep-Sea Research Part I: Oceanographic Research Papers*, *72*(0), 88–101. https://doi.org/10.1016/j.dsr.2012.10.010

Picheral, M., Guidi, L., Stemmann, L., Karl, D. M., Iddaoud, G., & Gorsky, G. (2010). The underwater vision profiler 5: An advanced instrument for high spatial resolution studies of particle size spectra and zooplankton. *Limnology and Oceanography: Methods*, *8*(SEPT), 462–473. https://doi.org/10.4319/lom.2010.8.462

Picheral, M., Catalano, C., Brousseau, D., Claustre, H., Coppola, L., Leymarie, E., et al. (2022). <scp>The Underwater Vision Profiler 6: an imaging sensor of particle size spectra and plankton, for autonomous and cabled platforms</scp>. *Limnology and Oceanography: Methods*, *20*(2), 115–129. https://doi.org/10.1002/lom3.10475

Ramondenc, S., Madeleine, G., Lombard, F., Santinelli, C., Stemmann, L., Gorsky, G., & Guidi, L. (2016). An initial carbon export assessment in the Mediterranean Sea based on drifting sediment traps and the Underwater Vision Profiler data sets. *Deep-Sea Research Part I: Oceanographic Research Papers*, *117*, 107–119. https://doi.org/10.1016/j.dsr.2016.08.015

Romanelli, E., Giering, S. L. C., Estapa, M., Siegel, D. A., & Passow, U. (2024). Can intense storms affect sinking particle dynamics after the North Atlantic spring bloom? *Limnology and Oceanography*, 2024.01.11.575202. https://doi.org/10.1002/lno.12723

Siegel, D., Burd, A., Estapa, M., Fields, E., Johnson, L., Romanelli, E., et al. (2024). Dynamics of Aggregates and Sinking Carbon Fluxes in a Turbulent Ocean. *EarthArXiv Eprints*. https://doi.org/10.31223/X58709

Siegel, D. A., Fields, E., & Buesseler, K. O. (2008). A bottom-up view of the biological pump: Modeling source funnels above ocean sediment traps. *Deep-Sea Research Part I: Oceanographic Research Papers*, *55*(1), 108–127. https://doi.org/10.1016/j.dsr.2007.10.006

Siegel, David A., Buesseler, K. O., Behrenfeld, M. J., Benitez-Nelson, C. R., Boss, E.,

Brzezinski, M. A., et al. (2016). Prediction of the export and fate of global ocean net primary production: The exports science plan. *Frontiers in Marine Science*, *3*(MAR). https://doi.org/10.3389/fmars.2016.00022

Siegel, David A., Cetinić, I., Graff, J. R., Lee, C. M., Nelson, N., Perry, M. J., et al. (2021). An operational overview of the EXport Processes in the Ocean from RemoTe Sensing (EXPORTS) Northeast Pacific field deployment. *Elementa: Science of the Anthropocene*, *9*(1). https://doi.org/10.1525/elementa.2020.00107

Siegel, David A., Cetinic, I., Thompson, A. F., Nelson, N. B., Sten, M., Omand, M., et al. (2023). *EXport Processes in the Ocean from RemoTe Sensing (EXPORTS) North Atlantic sensor calibration and intercalibration documents*. https://doi.org/10.1575/1912/66998

De Soto, F., Ceballos-Romero, E., & Villa-Alfageme, M. (2018). A microscopic simulation of particle flux in ocean waters: Application to radioactive pair disequilibrium. *Geochimica et Cosmochimica Acta*, *239*, 136–158. https://doi.org/10.1016/j.gca.2018.07.031

Stamieszkin, K., Steinberg, D. K., & Maas, A. E. (2021). Fecal pellet production by mesozooplankton in the subarctic Northeast Pacific Ocean. *Limnology and Oceanography*, *66*(7), 2585–2597. https://doi.org/10.1002/lno.11774

Steinberg, D. K., Stamieszkin, K., Maas, A. E., Durkin, C. A., Passow, U., Estapa, M. L., et al. (2023). The Outsized Role of Salps in Carbon Export in the Subarctic Northeast Pacific Ocean. *Global Biogeochemical Cycles*, *37*(1), e2022GB007523. https://doi.org/10.1029/2022GB007523

Stemmann, L., Jackson, G. A., & Ianson, D. (2004). A vertical model of particle size distributions and fluxes in the midwater column that includes biological and physical processes - Part I: Model formulation. *Deep-Sea Research Part I: Oceanographic Research Papers*, *51*(7), 865–884. https://doi.org/10.1016/j.dsr.2004.03.001

Trudnowska, E., Lacour, L., Ardyna, M., Rogge, A., Irisson, J. O., Waite, A. M., et al. (2021). Marine snow morphology illuminates the evolution of phytoplankton blooms and determines their subsequent vertical export. *Nature Communications*, *12*(1), 1–13. https://doi.org/10.1038/s41467-021-22994-4

941 Turner, J. (2002). Zooplankton fecal pellets, marine snow and sinking phytoplankton blooms.
942 *Aquatic Microbial Ecology*, *27*(1), 57–102. https://doi.org/10.3354/ame027057

943 Turner, J. T. (2015). Zooplankton fecal pellets, marine snow, phytodetritus and the ocean's
944 biological pump. *Progress in Oceanography*, *130*(1), 205–248.
945 https://doi.org/10.1016/j.pocean.2014.08.005

946 Werdell, P. J., & Bailey, S. W. (2002). The SeaWiFS Bio-optical Archive and Storage System
947 (SeaBASS): Current architecture and implementation, NASA Tech. Memo. 2002-211617 ,
948 G.S. Fargion and C.R. McClain, Eds., NASA Goddard Space Flight Center, Greenbelt,
949 Maryland, 45 pp. (2002). EXPORTS data:
950 https://doi.org/http://dx.doi.org/10.5067/SeaBASS/EXPORTS/DATA001

951 Whitney, F. A., Crawford, W. R., & Harrison, P. J. (2005). Physical processes that enhance
952 nutrient transport and primary productivity in the coastal and open ocean of the subarctic
953 NE Pacific. *Deep Sea Research Part II: Topical Studies in Oceanography*, *52*(5–6), 681–
954 706. https://doi.org/10.1016/j.dsr2.2004.12.023

955 Wong, C. S., Whitney, F. A., Iseki, K., Page, J. S., & Zeng, J. (1995). Analysis of trends in
956 primary productivity and chlorophyll-a over two decades at Ocean Station P (50 ….
957 *Canadian Journal of Fisheries and Aquatic Sciences*, *121*, 107–117. Retrieved from
958 http://www.ncbi.nlm.nih.gov/entrez/query.fcgi?db=pubmed&cmd=Retrieve&dopt=Abstract
959 Plus&list_uids=17746328481931740057%5Cnpapers2://publication/uuid/05C2F476-355C-
960 4812-9093-9EAE6218963D

961 Zhang, X., Huot, Y., Gray, D., Sosik, H. M., Siegel, D., Hu, L., et al. (2023). Particle size
962 distribution at Ocean Station Papa from nanometers to millimeters constrained with
963 intercomparison of seven methods. *Elementa: Science of the Anthropocene*, *11*(1).
964 https://doi.org/10.1525/elementa.2022.00094

Approach	# of size bins	size range	# camera casts	# trap deployments	trap depths (m)	#234Th profiles	type of data	A	CI	b	CI	r^2
Previous studies												
Kriest (2002) used by used by Kiko et al. (2017, 2020) for the size range 140 µm to 16.8 mm	nan	1000 µm – 10 mm	nan	nan	nan	nan	nan; nan; nan	16.49 ± nan	nan	2.24 ± nan	nan	nan
Guidi et al. (2008): classic UVP method	8	250 µm – 1.5 mm	118	11	100, 200, 300, 400, 1000	nan	S & C	12.50 ± 3.40	nan	3.81 ± 0.70	nan	0.73
Iversen et al. (2010) (using own, custom built camera system)	nan	150 µm – 6.5 mm	5	5	~ 1200, 1866	nan	S	273.8 ± nan	nan	4.27 ± nan	nan	0.74
Forest et al. (2013)	17	80 µm - 4.2 mm	> 154	21	~ 100, ~ 200	nan	C	28.1 ± 6.1	nan	2.0 ± 0.39	nan	0.68
Fender et al. (2019)	19	100 µm – 1.5 mm	~ 300	69	100-150	nan	S	15.40 ± nan	nan	1.05 ± nan	nan	nan
Clements et al. (2023)	23*	35 µm – 5 mm	8805	250	20-160	8805	C	18.0 ± 2.8	nan	2.63 ± 0.06	nan	0.51
This study												
Global approach using traps- 8 bins	8	250 µm – 1.5 mm	387	55	75-500	nan	S	15.44 ± 21.53	-6.08, 36.97	0.73 ± 1.55	-0.82, 2.29	0.79
Global approach using traps	23	128 µm – 26 mm	387	55	75-500	nan	S	13.21 ± 5.52	7.69, 18.74	1.54 ± 0.44	1.10, 1.98	0.81

Regional approach using traps NP	23	128 µm – 26 mm	169	23	100-500	nan	S	13.89 ± 7.75	6.14, 21.64	1.61 ± 0.69	0.92, 2.30	0.02
Regional approach using traps NA	23	128 µm – 26 mm	218	32	75-500	nan	S	12.46 ± 8.35	4.11, 20.81	1.48 ± 0.61	0.87, 2.09	0.82
Global approach using 234Th	23	128 µm – 26 mm	387	nan	nan	83	S	20.06± 2.88	17.18, 22.94	1.42 ± 0.15	1.26, 1.57	0.56
Regional approach using 234Th NP	23	128 µm – 26 mm	169	nan	nan	61	S	27.27 ± 3.42	23.85, 30.70	1.52 ± 0.15	1.37, 1.67	0.09
Regional approach using 234Th NA	23	128 µm – 26 mm	218	nan	nan	22	S	6.76 ± 4.24	2.52, 11.01	0.82 ± 0.48	0.34, 1.30	0.02

Table 1. Summary of A (in mg C m d^{-1} mm^{1-b}) and B coefficients with uncertainties and the r^2value for the linear fit from previous studies and this study. We provide the values and uncertainties of coefficients as reported by other authors and calculate the uncertainty for our A and b coefficients as the half-width of the interval of the values obtained. For our coefficients we provide the Confidence Interval (CI) as the ranges between the minimum and maximum values obtained for the coefficients. The numbers of size bins and the size range used for each approach are also reported along with the number of camera casts, number and depths of trap deployments, and number of ^{234}Th profiles when appropriate. The type of data used is specified, distinguishing between climatological (i.e., long-term data, denoted as C in the table) and simultaneous POC flux observations (denoted as S). Regarding previous studies, the A coefficient by Kriest (2002) was obtained from a relationship between size and nitrogen content of $273ESD^{1.62}$reported by Alldredge (1998) for miscellaneous aggregates (detritus, flagellates, etc.), while the b coefficient was calculated applying Stokes law assuming a sinking speed of 2.8 md^{-1} at 0.002 cm (see Tables 1 and 2 in Kriest (2002). Studies by Kiko et al. (2017, 2020) and Bisson et al. (2022) applied the same coefficients as by Kriest (2002). To obtain the coefficients by Guidi et al. (2008), from the 1254 UVP profiles available in their database only 118 data sets had both particle size distributions from the UVP and sediment trap flux measurements, see Table 3 in Guidi et al. (2008) for location, position and duration of the deployments of the sediment traps used in this study. Coefficients by Iversen et al. (2010) were obtained using a Particle Camera (ParCa) that illuminated a volume of 12.4 L (12 cm width) and was deployed only at night (see Table 2 in Iversen et al. (2010) for trap depth and collection periods).

*Forest et al. (2013) did not explicitly specify the number of UVP profiles and sediment trap deployments. However, the study covered 154 locations across the Mackenzie Shelf. UVP5 was mounted on the CTD rosette and deployed multiple times at each sampling station, with the number of deployments varying by station. The paper also indicates that there were 21 overlaps between sediment trap sampling and UVP5 deployments during the field campaign. Therefore, the minimum number of UVP and sediment trap deployments referenced in the study is 154 and 21, respectively.

†Clements et al. (2023) used the 23 size bins available for UVP5s, extending them to set the minimum size class to be 35 μm - below the detection limit of the UVP5 - because the power law slope has been shown to extend to this size range, and the maximum size to be 5 mm, which roughly corresponds to the size at which zooplankton become significant contributors to the particle biovolume detected by UVP5 in various regions. The shadowed area indicates the methods with low predictive power.

Supplementary Information

Contents of this file

Text S1

Table S1

Figures S1 to S6

Text S1.

UVP: data, sources, and calibration

1. UVP data

UVPs were deployed during EXPORTS to estimate the true particle population by means of measuring the PSD in the water column. Two UVP5s in EXPORTS-NP (serial numbers SN 201 and 207, see calibration report for more details, Siegel et al. (2023)), and three in EXPORTS-NA (SN 201, 203 and 205) provided high quality measurements of the abundance, composition, and size distribution of suspended particles (including live organisms) in the water column. During EXPORTS-NP, UVP5 SN207 captured data during CTD downcast during 138 of 144 casts of cruise *SR1812*; the unsuccessful casts did not have a clear cause as to why the instrument did not work as programmed. During cruise *RR1813*, UVP5 SN201 provided a total of 84 profiles of particle size distribution as part of the activities of the survey ship. During EXPORTS-NA, the UVP5s captured data during CTD downcast during 112, 69 and 13 casts of cruises DY131 (SN201), JC214 (SN203), and SdG2105 (SN205) respectively.

2. Data sources

NASA-funded primary data products are archived at *SeaWiFS Bio-optical Archive and Storage System* (*SeaBASS*). All EXPORTS data are being archived under one digital object identifier (DOI: http://dx.doi.org/10.5067/SeaBASS/EXPORTS/DATA001) that further expands into the individual data subsets.

For easier access and preliminary sharing, the 5m binned particle size data are also available in *EcoPart* (https://ecopart.obs-vlfr.fr/) and *EcoTaxa* (https://ecotaxa.obs-vlfr.fr/) with the following project names and numbers (3 digits for *EcoPart* and 4 digits for *EcoTaxa*) for the NP and NA experiments respectively:

- NP:
    - cruise *RR1813*: uvp5_sn201_exports_01_filtered(228) (*EcoTaxa* project 1286),
    - cruise *SR1812*: uvp5_sn207_2018_exports_np_sr1812_filtered(230) (*EcoTaxa* project 1591),
- NA:
    - cruise *JC224*: uvp5_sn201_exports02_filtered(473) (*EcoTaxa* project 5652),
    - cruise *DY131*: uvp5_sn203_ nasa_exports_north_atlantic_2021(371) (*EcoTaxa* project 4661), and
    - cruise *SdG2105*: uvp5_sn205_exports_2021_filtered(363) (*EcoTaxa* project 4521).

3. UVPs intercalibration

Calibration of the UVP5 pixel to millimeter conversion is done by the Laboratoire d'Océanographie de Villefranche sur Mer (LOV). This involves quantifying the illuminated volume and determining the appropriate conversion between imaged particle area in pixels and mm^2 (Picheral et al., 2010). The latter is initially done by measuring the size of particles with a microscope and their corresponding pixel area in the UVP image (dropping particles one at a time in the field of view of the camera) in order to determine the raw pixel size (pixels mm^{-1}). The instruments used during each EXPORTS cruise were sent together to the manufacturer for pre-cruise calibration, where each instrument underwent an in situ inter-calibration against the same reference UVP in the Bay of Villefranche, France. From this intercalibration, a power law relationship of the form $S_m = Aa \times S_p^{Exp}$ is used to derive calibration coefficients *Aa* and *Exp* for each instrument that minimize the log-transformed differences between the particle area in pixels (S_p) and particle area in mm^2 (S_m). These calibration coefficients are reported in the calibration documents and used to calculate the size of each particle imaged by the UVP during the EXPORTS program (see Siegel et al. (2023) for UVP calibration report).

As several UVP units were used, an intercalibration procedure was developed to allow comparability of data from these units. The full EXPORTS UVP intercalibration report can be found in (Siegel et al., 2023). Very briefly, the intercalibration procedure is based on a comparison between one or several reference units and the units to be calibrated. UVP-based PSD observations

1045 are intercompared using nearby in time and space casts. During EXPORTS-NP, UVP serial
1046 number 207 on the Survey Ship consistently overestimated the particle concentrations measured
1047 by UVP serial number 201 on the Process Ship for unknown reasons, despite being intercalibrated
1048 to a reference UVP prior to the cruise. These differences were observed across most size and depth
1049 bins. However, due to the limited number of intercomparison profiles and the fact that the
1050 instruments were not sampling the exact same parcels of water (deployed from separate ships), no
1051 specific corrections or adjustments were applied for EXPORTS-NP. An intermittent lighting issue,
1052 where at least one lighting unit failed to illuminate, was also noted for both UVP units. Bad images
1053 resulting from this issue were filtered out of the original database using a procedure developed by
1054 LOV. During EXPORTS-NA, four match-up casts were identified between *DY131* and *JC214* and
1055 two between the *DY131* and *SdG2105*. While *DY131* and *SdG2105* UVPs showed very similar
1056 PSD data; *JC214* PSD data were considerably lower, particularly for the smaller size bins, and had
1057 known issues related to the discovery of a zip tie in the field of view. *DY131* PSD data were used
1058 as the "standard" due to their consistent availability throughout the entire cruise and broad
1059 consistency with *SdG2105* PSD results. Linear regression models were employed to correct the
1060 *JC214* PSD data to best match the *DY131* data for the size bins with a linear correlation (r^2) value
1061 exceeding 0.8. The data were subsequently vertically binned into 25-m bins to enhance statistics
1062 for the largest size bins without significantly altering the values of the smaller bin corrections. The
1063 resulting remapped data show consistency among the three UVP-PSD data sources, offering a data
1064 set to explore the relationships among particle distributions and export fluxes.
1065

	NP			NA		
epoch	traps	UVP	234Th & UVP	traps	UVP	234Th & UVP
E1	11	37	17	7	17	5
E2	11	34	20	5	18	8
E3	10	73	18	6	9	9

Table S1. Summary of the number of UVP profiles, sediment traps, and ^{234}Th profiles used in the regional matchups by epoch.

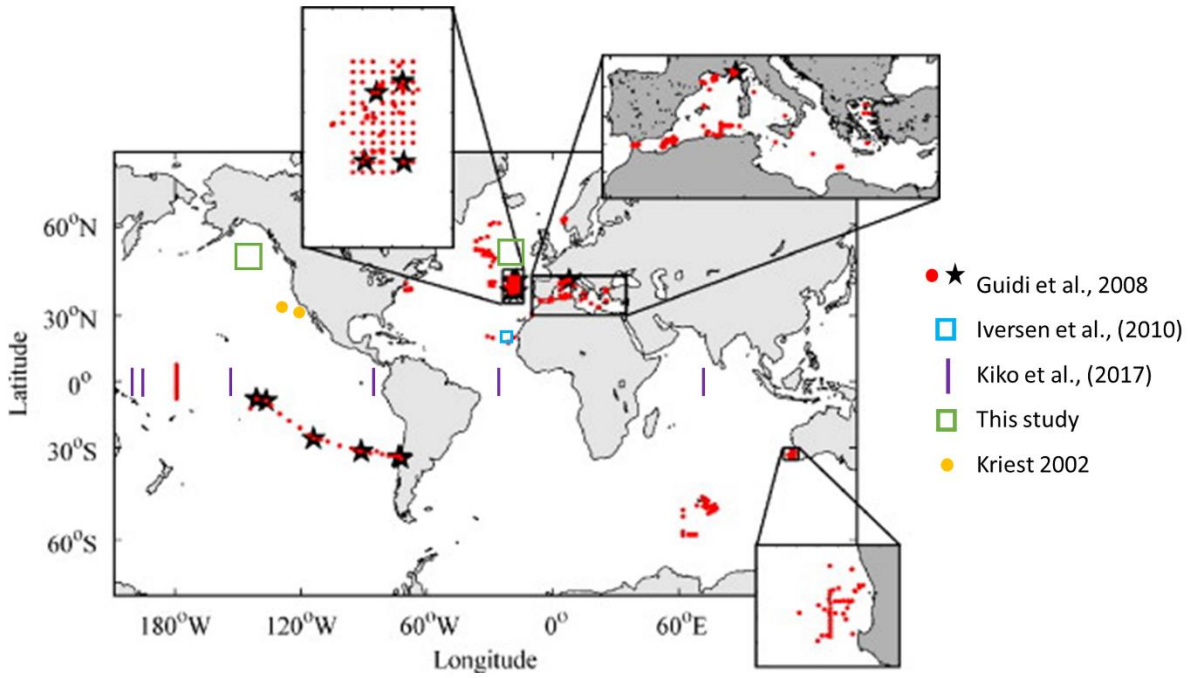

Figure S1. Modified map based on Figure 1 from Guidi et al., (2008) to include the sampling sites of the studies summarized in Table 1 that use observations to estimate A and B coefficients. The map features: red dots and black stars to indicate UVP and trap data respectively from Guidi et al., (2008), blue square to show study site from Iversen et al., (2010), sampled with deep sediment traps and an underwater camera (ParCa type), purple lines to indicate transits from Kiko et al., (2017) with UVP data, and green squares to denote sampling locations from this study, which included UVP data, and traps and ^{234}Th measurements. Kriest, (2002) estimated A and B coefficients based on a variety of observations about the mass and sinking speed of marine snow in relationship to its diameter from Alldredge (1998) and Smith et al., (1998). Sampling locations of these observations are indicated with yellow and orange circles respectively. Note that observations from Alldredge (1998) are based on undisturbed aggregates of marine snow hand-collected at depths of 10 to 20 m in the Santa Barbara Channel (California, USA), while those from Smith et al., (1998) are based on large detrital aggregates collected from the seafloor at an abyssal site in the NE Pacific. The observations used by Clements et al., (2023) are very extensive, and we therefore refer to the original publications for detailed sampling sites. Sediment traps and ^{234}Th locations used can be found in Figure 2 in Bisson et al., (2018), while the UVP data are available in Figure 2 in Kiko et al., (2022). The profiles of PSD observations used in Bisson et al., (2022) come from the first version of the UVP compilation by Kiko et al., (2022) accessible in (Kiko et al. (2021).

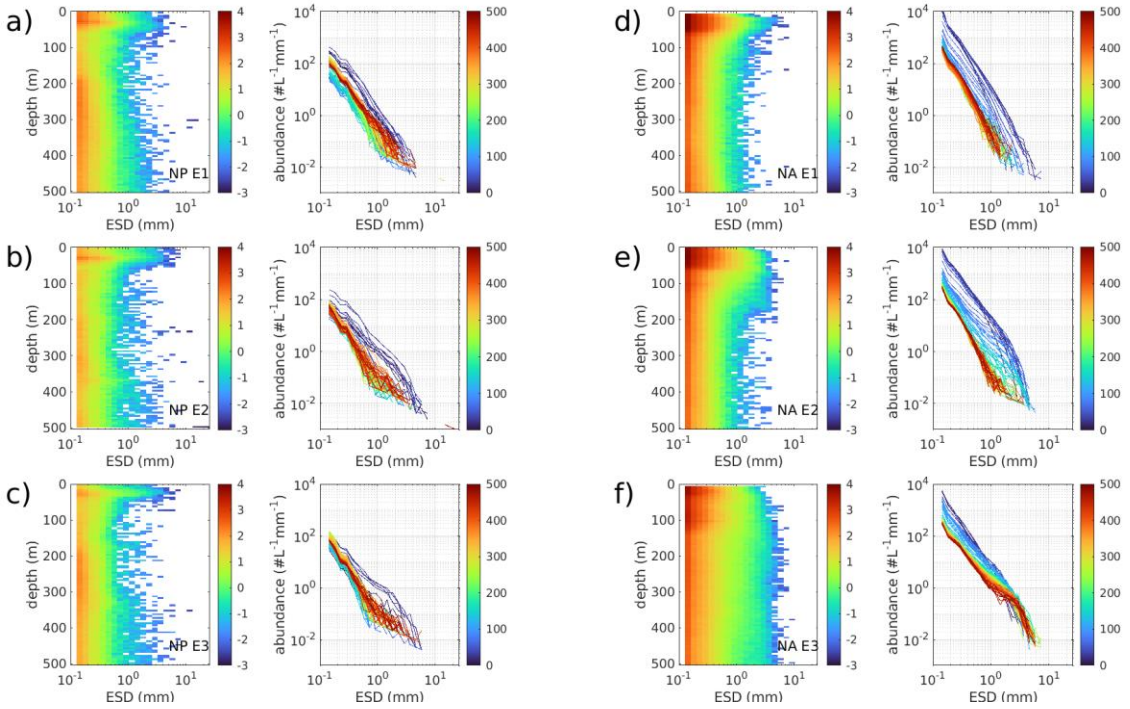

1086

1087 **Figure S2.** Observed particle size distribution (PSD) of in situ particles plotted against aggregate equivalent spherical
1088 diameter (ESD, mm) for the (a-c) NP and (d-f) NA experiments. For each panel, the figure on the left shows ESD
1089 versus depth, the color bar indicates particle abundance for each size (in # L^{-1} mm^{-1}, logarithmic scale). Red indicates
1090 a higher number of particles than blue; the figure on the right shows ESD versus abundance, the color bar indicates
1091 depth (in m). A random profile is shown for each of the epochs (E1, E2, and E3).

1092

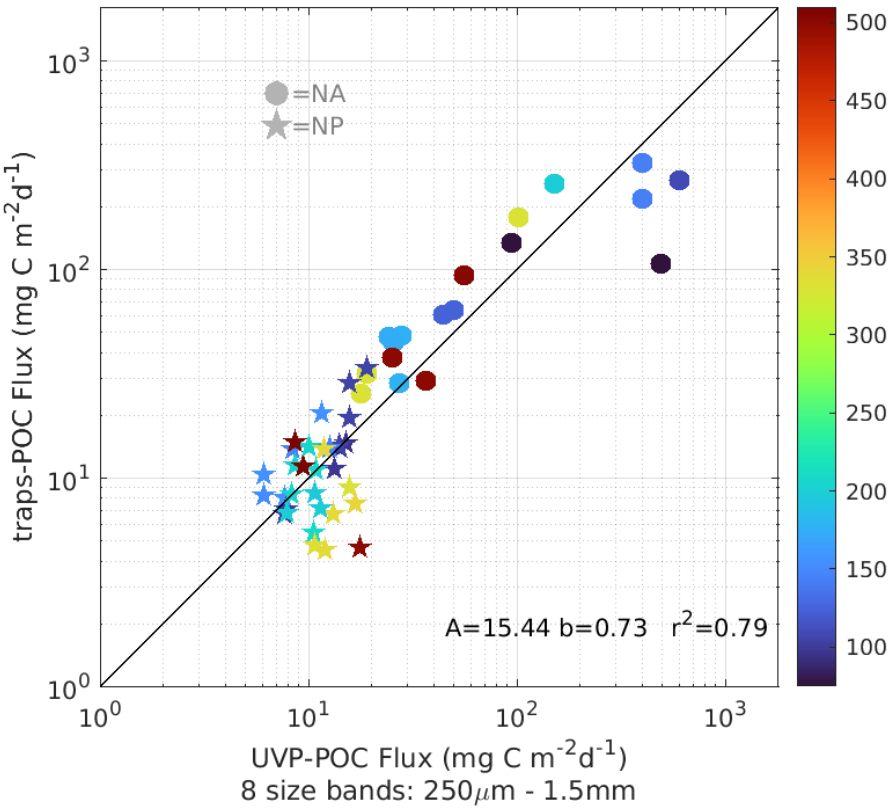

Figure S3. Detailed figure for our reproduction of the "classic UVP method" with the EXPORTS data set (i.e., global approach using traps with 8 bins). Color coding indicates depth.

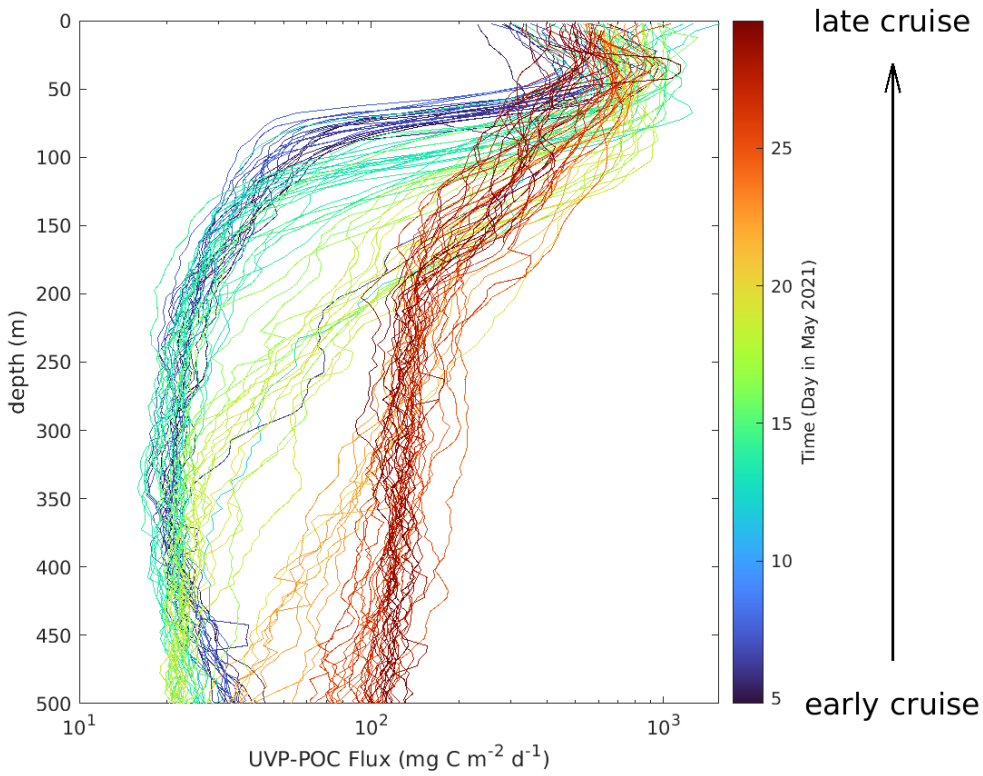

Figure S4. Vertical profiles of POC fluxes for the global approach in the NA using trap data (Figure 4a in the main text) featuring color as time, with blue corresponding to early in the cruise and red with late in the cruise.